Initial Characterization of Active Transitioning Centaur, P/2019 LD$_2$ (ATLAS), Using Hubble, Spitzer, ZTF, Keck, Apache Point Observatory, and GROWTH Visible and Infrared Imaging and Spectroscopy

Bryce T. Bolin[1,2], Yanga R. Fernandez[3], Carey M. Lisse[4], Timothy R. Holt[5,6], Zhong-Yi Lin[7], Josiah N. Purdum[8], Kunal P. Deshmukh[9], James M. Bauer[10], Eric C. Bellm[11], Dennis Bodewits[12], Kevin B. Burdge[1], Sean J. Carey[2], Chris M. Copperwheat[13], George Helou[2], Anna Y. Q. Ho[1], Jonathan Horner[5], Jan van Roestel[1], Varun Bhalerao[14], Chan-Kao Chang[7], Christine Chen[15,16], Chen-Yen Hsu[7], Wing-Huen Ip[7], Mansi M. Kasliwal[1], Frank J. Masci[2], Chow-Choong Ngeow[7], Robert Quimby[8,17], Rick Burruss[18], Michael Coughlin[19], Richard Dekany[18], Alexandre Delacroix[18], Andrew Drake[1], Dmitry A. Duev[1], Matthew Graham[1], David Hale[18], Thomas Kupfer[20], Russ R. Laher[2], Ashish Mahabal[1,21], Przemyslaw J. Mróz[1], James D. Neill[1], Reed Riddle[19], Hector Rodriguez[19], Roger M. Smith[19], Maayane T. Soumagnac[22,23], Richard Walters[1], Lin Yan[24], and Jeffry Zolkower[18]

[1] Division of Physics, Mathematics and Astronomy, California Institute of Technology, Pasadena, CA 91125, USA; bbolin@caltech.edu
[2] IPAC, Mail Code 100-22, Caltech, 1200 E. California Blvd., Pasadena, CA 91125, USA
[3] Department of Physics, University of Central Florida, Orlando, FL 32816, USA
[4] Johns Hopkins University Applied Physics Laboratory, Laurel, MD 20723, USA
[5] Centre for Astrophysics, University of Southern Queensland, West St., Toowoomba, QLD 4350, Australia
[6] Southwest Research Institute, Department of Space Studies, Boulder, CO 80302, USA
[7] Graduate Institute of Astronomy, National Central University, 32001, Taiwan
[8] Department of Astronomy, San Diego State University, 5500 Campanile Dr., San Diego, CA 92182, USA
[9] Department of Metallurgical Engineering and Materials Science, Indian Institute of Technology Bombay, Powai, Mumbai-400076, India
[10] Department of Astronomy, University of Maryland, College Park, MD 20742-0001, USA
[11] DIRAC Institute, Department of Astronomy, University of Washington, 3910 15th Ave. NE, Seattle, WA 98195, USA
[12] Physics Department, Leach Science Center, Auburn University, Auburn, AL 36832, USA
[13] Astrophysics Research Institute Liverpool John Moores University, 146 Brownlow Hill, Liverpool L3 5RF, UK
[14] Department of Physics, Indian Institute of Technology Bombay, Powai, Mumbai-400076, India
[15] Space Telescope Science Institute (STScI), 3700 San Martin Dr., Baltimore, MD 21218, USA
[16] Department of Physics and Astronomy, The Johns Hopkins University, 3701 San Martin Dr., Baltimore, MD 21218, USA
[17] Kavli Institute for the Physics and Mathematics of the Universe (WPI), The University of Tokyo Institutes for Advanced Study, The University of Tokyo, Kashiwa, Chiba 277-8583, Japan
[18] Caltech Optical Observatories, California Institute of Technology, Pasadena, CA 91125, USA
[19] School of Physics and Astronomy, University of Minnesota, Minneapolis, MN 55455, USA
[20] Kavli Institute for Theoretical Physics, University of California, Santa Barbara, CA 93106, USA
[21] Center for Data Driven Discovery, California Institute of Technology, Pasadena, CA 91125, USA
[22] Lawrence Berkeley National Laboratory, 1 Cyclotron Rd., Berkeley, CA 94720, USA
[23] Department of Particle Physics and Astrophysics, Weizmann Institute of Science, Rehovot 76100, Israel
[24] The Caltech Optical Observatories, California Institute of Technology, Pasadena, CA 91125, USA

Abstract

We present visible and mid-infrared imagery and photometry of temporary Jovian co-orbital comet P/2019 LD$_2$ taken with Hubble Space Telescope/Wide Field Camera 3 (HST/WFC3), Spitzer Space Telescope/Infrared Array Camera (Spitzer/IRAC), and the GROWTH telescope network, visible spectroscopy from Keck/Low-Resolution Imaging Spectrometer (LRIS), and archival Zwicky Transient Facility observations taken between 2019 April and 2020 August. Our observations indicate that the nucleus of LD$_2$ has a radius between 0.2 and 1.8 km assuming a 0.08 albedo and a coma dominated by $\sim$100 μm-scale dust ejected at $\sim$1 m s^{-1} speeds with a $\sim$1′ jet pointing in the southwest direction. LD$_2$ experienced a total dust mass loss of $\sim$10^8 kg at a loss rate of $\sim$6 kg s^{-1} with Afρ/ cross section varying between $\sim$85 cm/125 km^2 and $\sim$200 cm/310 km^2 from 2019 April 9 to 2019 November 8. If the increase in Afρ/cross section remained constant, it implies LD$_2$'s activity began $\sim$2018 November when within 4.8 au of the Sun, implying the onset of H$_2$O sublimation. We measure CO/CO$_2$ gas production of $\lesssim$10^{27} mol s^{-1}/$\lesssim$10^{26} mol s^{-1} from our 4.5 μm Spitzer observations; g–$r = 0.59 \pm 0.03$, r–$i = 0.18 \pm 0.05$, and i–$z = 0.01 \pm 0.07$ from GROWTH observations; and H$_2$O gas production of $\lesssim$80 kg s^{-1} scaling from our estimated C_2 production of $Q_{C_2} \lesssim 7.5 \times 10^{24}$ mol s^{-1} from Keck/LRIS spectroscopy. We determine that the long-term orbit of LD$_2$ is similar to Jupiter-family comets having close encounters with Jupiter within $\sim$0.5 Hill radius in the last $\sim$3 y and within 0.8 Hill radius in $\sim$9 y. Additionally, 78.8% of our orbital clones are ejected from the solar system within 1×10^6 yr, having a dynamical half-life of 3.4×10^5 yr.

Unified Astronomy Thesaurus concepts: Celestial mechanics (211); Centaurs (215); Short period comets (1452)

1. Introduction

The gas giant Jupiter is the dominant gravitational perturbing body affecting the dynamical transfer of solar system comets from the outer solar system's trans-Neptunian disk beyond the orbit of Neptune into the inner reaches of the solar system (recently described in Dones et al. 2015). The vast majority of comets transfer from the outer solar system regions such as the Oort Cloud in the case of long-period comets (recently

described in Vokrouhlický et al. 2019) or the trans-Neptunian region in the case of short-period comets (recently described in Nesvorný et al. 2017). Once the comets originating from the trans-Neptunian region randomly walk their way through the outer solar system and become strongly influenced by close encounters with Neptune and Uranus, a significant portion are transformed in their orbital configuration into the Centaur group of small bodies. The Centaur class is defined as having semimajor axes, a, and perihelion, q, between 5.2 au, the semimajor axis a_J of Jupiter, and 30 au, the semimajor axis of Neptune, a_N (Jewitt 2009). An additional quantity used to define the small bodies in the inner solar system is the Tisserand parameter with respect to Jupiter, T_J, defined as

$$T_J = \frac{a_J}{a} + 2\sqrt{(1 - e^2)\frac{a}{a_J}}\cos i \qquad (1)$$

where e is the eccentricity of the body and i is the inclination. The parameter T_J can be used as a rough indication of how much an object is influenced by the gravitational perturbations of Jupiter (Murray & Dermott 1999). Centaurs are objects that generally have $T_j > 3.05$ (Gladman et al. 2008), whereas Jupiter-family comets have $3 > T_J > 2$ (Duncan et al. 2004). However, we note that the $T_j > 3.05$ boundary does not strictly define objects as Centaurs as there can be non-Centaur objects with $T_j > 3.05$.

The mean dynamical half-life of Centaurs is $\sim$2.7 Myr, with the vast majority of Centaurs eventually being ejected from the solar system (Horner et al. 2004b), while the Jupiter-family comets have a bit shorter lifetimes of $\sim$0.5 Myr (Levison & Duncan 1994). The chaotic evolution of the Centaurs causes a significant number (around one-third) to become Jupiter-family comets at some point in their lifetimes, prior to their eventual ejection from the solar system (Horner et al. 2004a). The Centaur 2014 OG_{392}, recently discovered to be active (Chandler et al. 2020), may be an example of an object transitioning between the Centaur and Jupiter-family comet groups. Some can even be temporarily captured as satellites of the giant planets, or by the Jovian and Neptunian Trojan populations (e.g., Horner & Evans 2006; Horner & Lykawka 2012). Another example of a Centaur recently in the stage of becoming a Jupiter-family comet is 29P/ Schwassmann-Wachmann. Centaur 29P is located in a region of orbital parameter space with 5.5 au $< q <$ 8.0 au and aphelion 5 au $< Q <$ 7 au that acts as a "gateway" that the Centaurs preferentially inhabit while in the process of dynamically transferring to become Jupiter-family comets (Sarid et al. 2019).

The recently discovered, briefly Jovian co-orbital comet P/ 2019 LD_2 (Sato et al. 2020), with a semimajor axis of 5.30 au, a perihelion of 4.57 au, and aphelion of 6.02 au, may be another example of an object in the transition region between Centaur objects and Jupiter-family comets. The comet will only spend about one orbit in the dynamical configuration where it has a Jupiter-similar semimajor axis (Hsieh et al. 2021; Kareta et al. 2020a). Initially reported as an inactive object by the ATLAS survey (Tonry 2011) in 2019 June and designated by the Minor Planet Center as 2019 LD_2,[25] it was discovered to be active by amateur astronomers.[26] Prediscovery images and follow-up

images of the comet taken by ATLAS and other ground-based telescopes resulted in it being given the cometary designation P/2019 LD_2 (Fitzsimmons et al. 2020). While technically some of the orbital elements of P/2019 LD_2, such as its semimajor axis, resemble those of a Jovian co-orbital, it is inherently unstable, in stark contrast to the stable orbits of Jovian Trojans, which are stable on timescales comparable to the age of the solar system and are located at $\sim \pm$ 60° mean longitude with respect to Jupiter (e.g., Marzari et al. 2002). In addition, the Jovian Trojans have a different origin, having most likely been captured as a result of Jupiter's migration during the solar system's formation, 4.5 Gyr ago (e.g., Morbidelli et al. 2005; Roig & Nesvorný 2015).

One proposed origin for P/2019 LD_2 is that it is a Jupiter-family comet in the transition region in orbital parameter space inhabited by objects that are in transition between Centaurs and Jupiter-family comets (Steckloff et al. 2020). As comets transfer from their origins in the outer solar system beyond the orbit of Neptune and become denizens of the inner solar system, they will experience a dramatic shift in thermal environment, due to increased thermal insolation from the Sun (De Sanctis et al. 2000; Sarid & Prialnik 2009). The consequence of the increased solar insolation as the comet nears the Sun is the increased heating and sublimation of volatiles such as CO and H_2O near the comet's surface (Meech & Svoren 2004). Another consequence of the increased heating from closer proximity to the Sun is that large-scale ablation of the comet's structure due to thermal stress can occur, resulting in it becoming partially or completely disrupted (Fernández 2009). Since P/2019 LD_2 is now in transition between the Centaur and Jupiter-family comet populations, it seems likely that it has become active for the first time, and as such, its activity will be rapidly evolving in response to the new epoch of increased solar heating.

We therefore present in this paper an analysis of visible-light, high-resolution Hubble Space Telescope/Wide Field Camera 3 (HST/WFC3; Dressel 2012) observations of P/2019 LD_2 using the approach of Jewitt et al. (2014) and Bolin & Lisse (2020) to understand the dust coma and nucleus properties, and to constrain the cause of P/2019 LD_2's activity. We will also use mid-infrared (MIR) P/2019 LD_2 observations taken with the Spitzer Space Telescope/Infrared Array Camera (Spitzer/IRAC; Werner et al. 2004) combined with the analysis techniques of Reach et al. (2013) and Lisse et al. (2020) to place upper limits on the comet's $CO+CO_2$ gas production. We also use multiwavelength observations covering the visible and MIR by building on the techniques of Bolin et al. (2020b) by using a network of ground-based observatories to characterize the physical properties of this transitioning Centaur. In addition, we will examine the long-term orbital properties of P/2019 LD_2 using its latest orbital solution in order to better understand its possible origins and future dynamical evolution.

2. Observations

Observations of P/2019 LD_2 were obtained before the official announcement of its activity in 2020 May both by targeted observations by ground- and space-based observatories and serendipitously in the survey observations by the Zwicky Transient Facility (ZTF; Graham et al. 2019). The time span of our targeted observations is 2019 September 7 UTC to 2020 August 19 UTC, including observations by the Astrophysical Research Consortium 3.5 m telescope (ARC 3.5 m),

---

Table 1
Summary of P/2019 LD$_2$ Target Observations Viewing Geometry

Date[1] UTC	Facility[2]	Filter[3]	θ_s^4 ('')	χ_{am}^5	r_H^6 (au)	Δ^7 (au)	α^8 (°)	δ_E^9 (°)	$T - T_p^{10}$ (days)
2019 Apr 26	ZTF[a]	r	2.17	1.76	4.693	4.147	10.99	−1.56	−343.97
2019 Sep 07	ARC	g,r	1.4	1.81	4.622	4.279	12.23	−0.74	−216.58
2020 Jan 25–26	Spitzer	4.5 μm	⋯	⋯	4.584	4.256[b]	12.61[b]	0.23[b]	−76.58
2020 Apr 01	HST	F350LP	⋯	⋯	4.578	5.023	10.71	−0.44	−9.58
2020 May 27	MLO 1.0-m	B,V,R	1.92	1.49	4.580	4.221	12.38	−2.50	46.42
2020 May 29	LT	g,r,i,z	1.21	1.75	4.580	4.193	12.27	−2.56	48.42
2020 June 23–27	LOT	B,V,R	1.47	1.14	4.583	3.848	9.59	−3.00	75.42
2020 July 10	LOT	B,V,R	1.45	1.15	4.586	3.707	7.11	−2.97	90.42
2020 Aug 19	Keck I	Sp.[c]	0.85	1.80	4.594	3.608	3.20	−1.76	130.42

Notes. Columns: (1) observation date; (2) observational facility; (3) filter (for the Keck I observations, the B600/4000 grism and R600/7500 grating are used with the Low-Resolution Imaging Spectrometer instrument[c]); (4) in-image seeing of observations; (5) air mass of observations; (6) heliocentric distance; (7) topocentric distance; (8) phase angle; (9) topocentric and target orbital plane angle; (10) difference between time of observation T and time of perihelion T_p.
[a] Serendipitous observation of P/2019 LD$_2$ with ZTF, but included in this table because of its inclusion in the top left panel of Figure 1.
[b] *Spitzer*-centric.
[c] https://www2.keck.hawaii.edu/inst/lris/dispersive_elements.html

Spitzer, HST, Keck I, and members of the GROWTH network (Kasliwal et al. 2019), such as the Mount Laguna Observatory 40 inch Telescope (MLO 1.0 m), Liverpool Telescope (LT), and Lulin Optical Telescope (LOT). A list of our targeted observations and their viewing geometry are provided in Table 1. The time span of our serendipitous observations of P/2019 LD$_2$ made with the ZTF survey is between 2019 April 9 UTC and 2019 November 8 UTC, and the photometry data are listed with the viewing geometry in Table 2.

2.1. Zwicky Transient Facility

We searched for serendipitous observations of P/2019 LD$_2$ made with the Zwicky Transient Facility survey mounted on the Palomar Observatory's 48 inch telescope (Bellm et al. 2019) in the ZTF archive (Masci et al. 2019). The ZTF archive possessed observations of P/2019 LD$_2$ made as far back as 2019 April 9 UTC, which we include up to 2019 November 8 UTC. The observations were made in the g and r bands in images consisting of 30 s exposures. Seeing conditions were typically between 1$\farcs$5 and 2$\farcs$5 and at air masses ranging from 1.4 to 2.6. A full list of observations of P/2019 LD$_2$ made by ZTF containing the viewing geometry and observing conditions is presented in Table 2.

2.2. Apache Point Astrophysical Research Consortium 3.5 m

Following the announcement of the appearance of activity of P/2019 LD$_2^2$ (then called 2019 LD$_2$), we triggered target-of-opportunity observations with the ARC 3.5 m telescope at Apache Point Observatory (APO) on 2019 September 7 UTC using the ARCTIC large-format optical CCD camera (Huehnerhoff et al. 2016). The camera was used in full-frame, quad amplifier readout, 2 × 2 binning mode, resulting in a pixel scale of 0$\farcs$228, and it was used with the g and r filters. In total, 14 g and r exposures were obtained, each 120 s long and in alternating order between the g and r filters. The telescope was tracked at the sky-motion rate of the comet of 8$\farcs$6 hr^{-1}. The seeing was 1$\farcs$4 and the air mass was 1.8 during the observations.

2.3. Spitzer Space Telescope

Observations of P/2019 LD$_2$ were made with the Spitzer Space Telescope (Spitzer) using the IRAC instrument (Fazio et al. 2004) on 2020 January 25–26 UTC (DDT program 14331, PI Bolin et al. 2019). The observations consisted of 11 Astronomical Observing Requests (AORs), each consisting of 80 × 12 s dithered frames and having a ∼0.44 hr duration for a total of 4.8 hr clock time. The frames where dithered in groups of 10, with each using a large cycling pattern. The sky at the location of P/2019 LD$_2$ during the Spitzer observations possessed a high density of stars due to its low −18° galactic latitude, so shadow observations were used to improve the sensitivity of the observations. Out of a total of 11 AORs, eight were focused on the observed P/2019 LD$_2$, for a total of 2.13 hr of on-source time. The remaining three AORs were shadow observations that were evenly spaced in the sky location covering the trajectory of P/2019 LD$_2$ during 2020 January 02:23:32–23:10:44 that P/2019 LD$_2$ was being observed. The target was centered in the 4.5 μm channel because this channel is sensitive to CO/CO_2 emission and also because the object was expected to be the brightest at this wavelength. The 4.5 μm IRAC channel has a spatial resolution of 1$\farcs$2 pixel^{-1}. The data were reduced in a method as described in Fernández et al. (2013).

2.4. Hubble Space Telescope

The *Hubble Space Telescope* was used to observe P/2019 LD$_2$ with General Observer's (GO) time on 2020 April 1 UTC (HST GO 16077, PI Bolin et al. 2020a). During the one orbit visit, five 380 s F350LP filter exposures were obtained with the UVIS2 array of the WFC3/UVIS camera (Dressel 2012) for a total of 1900 s of integration time over a single orbit. The F350LP filter has a central wavelength of 582 nm with an FWHM bandpass of 490 nm (Deustua et al. 2017). The instrument and filter combination of WFC3 and the F350LP filter provides a per-pixel resolution of 0$\farcs$04 corresponding to 145 km at the topocentric distance of the comet. The comet was tracked nonsidereally according to its sky-plane rate of motion of 40$''$ hr^{-1}.

Table 2
Summary of ZTF P/2019 LD$_2$ Photometry

Date[1] UTC	r_H^2 (au)	Δ^3 (au)	α^4 (°)	$T - T_p^5$ (days)	Filter[6]	mag[7]	σ_{mag}^8	θ_s^9 (″)	χ_{am}^{10}	A(0°)fρ^{11} (cm)	C[12] (km^2)
2019 Apr 09-10:32	4.704	4.391	12.0	−360.20	r	19.33	0.15	2.36	1.72	85.28	127.69
2019 Apr 12-10:32	4.702	4.345	11.9	−357.32	r	19.27	0.16	2.83	1.66	87.90	131.53
2019 Apr 15-09:59	4.700	4.300	11.7	−354.47	r	19.13	0.15	1.82	2.02	97.23	145.35
2019 Apr 20-09:33	4.697	4.227	11.4	−349.70	r	18.97	0.23	1.87	1.83	107.69	160.77
2019 Apr 20-10:04	4.697	4.226	11.4	−349.68	r	18.83	0.23	2.44	1.51	122.45	182.81
2019 Apr 26-09:00	4.693	4.142	11.0	−343.97	g	19.69	0.14	2.14	1.91	83.20	124.00
2019 Apr 26-09:07	4.693	4.142	11.0	−343.96	g	19.38	0.13	2.18	2.12	110.69	164.97
2019 Apr 26-11:26	4.693	4.141	11.0	−343.87	r	18.89	0.07	1.90	1.41	109.63	163.38
2019 Apr 26-11:36	4.693	4.141	11.0	−343.86	r	19.18	0.07	1.68	1.37	83.93	125.08
2019 May 02-10:03	4.689	4.061	10.4	−338.17	r	18.95	0.11	2.47	1.56	97.64	145.18
2019 May 02-10:32	4.689	4.061	10.4	−338.15	r	18.99	0.09	1.82	1.41	94.11	139.93
2019 May 31-08:22	4.672	3.763	6.1	−310.33	r	18.76	0.07	1.60	1.44	85.34	125.82
2019 May 31-10:34	4.672	3.762	6.1	−310.24	g	18.96	0.07	1.79	1.44	112.44	165.78
2019 Jun 01-09:04	4.671	3.755	6.0	−309.33	r	18.57	0.05	1.78	1.38	100.81	148.64
2019 Jun 02-09:34	4.671	3.748	5.8	−308.35	r	18.49	0.07	2.53	1.37	107.32	158.24
2019 Jun 02-10:57	4.671	3.748	5.8	−308.29	g	18.95	0.08	1.93	1.52	111.35	164.18
2019 Jun 03-11:33	4.670	3.741	5.6	−307.30	g	18.52	0.18	1.99	1.71	163.56	241.16
2019 Jun 04-07:01	4.670	3.736	5.5	−306.52	r	18.06	0.06	2.07	1.67	156.64	230.96
2019 Jun 04-08:31	4.670	3.736	5.5	−306.46	g	18.68	0.09	2.55	1.40	140.25	206.79
2019 Jun 06-06:37	4.668	3.725	5.1	−304.60	r	18.36	0.08	1.99	1.77	116.28	171.48
2019 Jun 06-08:33	4.668	3.724	5.1	−304.53	g	18.63	0.09	2.11	1.39	143.63	211.82
2019 Jun 07-09:33	4.668	3.719	4.9	−303.52	r	18.14	0.06	1.87	1.39	140.87	207.78
2019 Jun 08-06:36	4.667	3.714	4.8	−302.67	r	18.57	0.09	1.90	1.73	94.15	138.88
2019 Jun 08-09:12	4.667	3.713	4.8	−302.57	g	18.56	0.08	2.07	1.37	150.52	222.03
2019 Jun 09-06:36	4.667	3.709	4.6	−301.71	r	18.38	0.06	1.89	1.70	111.02	163.79
2019 Jun 10-07:02	4.666	3.704	4.5	−300.72	r	18.34	0.06	1.90	1.56	114.39	168.78
2019 Jun 10-08:03	4.666	3.704	4.5	−300.68	g	18.70	0.10	2.27	1.40	130.13	192.01
2019 Jun 11-09:43	4.666	3.699	4.3	−299.65	g	18.90	0.10	1.93	1.42	107.13	158.11
2019 Jun 14-08:02	4.664	3.688	3.9	−296.81	g	18.74	0.22	2.03	1.38	121.43	179.30
2019 Jun 20-07:50	4.661	3.673	3.3	−291.02	g	18.61	0.22	2.51	1.38	132.47	195.84
2019 Jun 20-08:17	4.661	3.673	3.3	−291.00	r	18.15	0.10	1.97	1.37	127.68	188.75
2019 Jun 23-09:02	4.659	3.669	3.2	−288.07	r	18.23	0.08	2.41	1.43	117.79	174.17
2019 Jun 23-10:34	4.659	3.669	3.2	−288.00	g	18.77	0.18	2.57	1.84	113.53	167.87
2019 Jun 26-07:37	4.657	3.667	3.2	−285.22	r	18.21	0.05	1.87	1.37	119.75	177.06
2019 Jun 26-08:02	4.657	3.667	3.2	−285.20	g	18.80	0.08	2.19	1.38	110.22	162.98
2019 Jul 01-06:45	4.655	3.671	3.5	−280.41	r	18.33	0.05	1.84	1.40	108.62	160.51
2019 Jul 01-06:46	4.655	3.671	3.5	−280.41	r	18.33	0.05	1.77	1.39	108.62	160.51
2019 Jul 01-07:44	4.655	3.671	3.5	−280.37	r	18.34	0.06	2.37	1.38	107.63	159.04
2019 Jul 01-07:44	4.655	3.671	3.5	−280.37	r	18.34	0.06	2.18	1.38	107.63	159.04
2019 Jul 03-07:10	4.654	3.674	3.8	−278.45	r	18.17	0.05	2.31	1.37	127.49	188.29
2019 Jul 03-07:32	4.654	3.674	3.8	−278.44	g	18.58	0.07	2.14	1.37	138.51	204.56
2019 Jul 04-07:36	4.653	3.676	3.9	−277.46	r	18.09	0.05	2.04	1.38	137.86	203.57
2019 Jul 06-06:43	4.652	3.681	4.2	−275.56	g	18.74	0.09	1.92	1.38	121.73	179.68
2019 Jul 08-07:32	4.651	3.687	4.5	−273.59	g	18.48	0.07	1.92	1.39	156.89	231.49
2019 Jul 09-05:29	4.651	3.690	4.6	−272.70	r	18.13	0.04	1.58	1.48	137.39	202.69
2019 Jul 09-07:36	4.651	3.690	4.6	−272.61	g	18.61	0.07	1.84	1.40	139.94	206.46
2019 Jul 10-06:01	4.650	3.694	4.8	−271.71	r	18.21	0.06	2.02	1.41	128.82	190.02
2019 Jul 10-06:02	4.650	3.694	4.8	−271.71	r	18.06	0.06	2.30	1.41	147.90	218.17
2019 Jul 10-06:13	4.650	3.694	4.8	−271.70	r	18.27	0.06	1.96	1.39	121.89	179.80
2019 Jul 10-06:31	4.650	3.694	4.8	−271.69	r	18.20	0.07	2.44	1.38	130.01	191.77
2019 Jul 10-06:41	4.650	3.694	4.8	−271.68	r	18.15	0.05	2.04	1.37	136.14	200.81
2019 Jul 10-06:42	4.650	3.694	4.8	−271.68	r	18.18	0.06	2.14	1.37	132.43	195.34
2019 Jul 11-07:29	4.649	3.698	4.9	−270.68	g	18.70	0.13	1.90	1.40	130.73	192.82
2019 Jul 12-06:32	4.649	3.702	5.1	−269.74	r	18.23	0.11	2.46	1.37	128.40	189.36
2019 Jul 12-06:33	4.649	3.702	5.1	−269.74	r	18.25	0.10	2.35	1.37	126.06	185.90
2019 Jul 12-07:24	4.649	3.702	5.1	−269.71	g	18.53	0.15	2.01	1.40	154.37	227.66
2019 Jul 13-06:03	4.648	3.706	5.3	−268.79	r	18.12	0.10	2.49	1.39	143.40	211.46
2019 Jul 13-07:51	4.648	3.707	5.3	−268.72	g	18.80	0.24	1.69	1.45	121.56	179.25
2019 Jul 16-05:21	4.647	3.721	5.8	−265.91	g	18.57	0.28	2.10	1.39	154.15	227.28
2019 Jul 16-06:32	4.647	3.721	5.8	−265.86	r	18.26	0.16	1.92	1.39	129.40	190.79
2019 Jul 20-06:54	4.645	3.745	6.5	−261.96	g	18.65	0.16	2.67	1.45	148.69	219.26
2019 Jul 21-05:12	4.645	3.751	6.6	−261.05	r	18.22	0.04	1.52	1.38	140.36	206.99
2019 Jul 21-05:13	4.645	3.751	6.6	−261.05	r	18.18	0.04	1.58	1.38	145.63	214.76

Table 2
(Continued)

Date[1] UTC	r_H^2 (au)	Δ^3 (au)	α^4 (°)	$T - T_p^5$ (days)	Filter[6]	mag[7]	σ_{mag}^8	θ_s^9 (″)	χ_{am}^{10}	A(0°)$f\rho^{11}$ (cm)	C[12] (km²)
2019 Jul 21-05:43	4.644	3.751	6.6	−261.03	r	18.17	0.05	1.44	1.37	146.91	216.66
2019 Jul 21-06:07	4.644	3.751	6.7	−261.01	r	18.34	0.05	1.46	1.38	126.07	185.94
2019 Jul 21-06:44	4.644	3.752	6.7	−260.99	r	18.35	0.09	2.67	1.43	124.98	184.33
2019 Jul 21-06:44	4.644	3.752	6.7	−260.99	r	18.31	0.08	2.71	1.44	129.68	191.25
2019 Jul 30-06:02	4.640	3.820	8.2	−252.26	r	18.21	0.05	1.85	1.42	155.19	229.33
2019 Jul 30-06:03	4.640	3.820	8.2	−252.26	r	18.20	0.04	1.70	1.42	156.63	231.45
2019 Jul 30-06:29	4.640	3.820	8.2	−252.24	r	18.27	0.05	1.92	1.49	146.85	217.00
2019 Jul 30-06:30	4.640	3.820	8.2	−252.24	r	18.30	0.05	1.82	1.49	142.85	211.08
2019 Aug 03-04:02	4.638	3.856	8.8	−248.45	r	18.31	0.10	1.65	1.40	147.13	217.68
2019 Aug 12-03:38	4.634	3.949	10.0	−239.69	r	18.11	0.16	3.23	1.39	192.88	286.40
2019 Aug 16-07:30	4.632	3.996	10.5	−235.63	r	18.34	0.16	1.83	1.78	162.34	241.48
2019 Aug 19-03:27	4.631	4.030	10.8	−232.87	r	18.33	0.09	1.41	1.38	168.23	250.52
2019 Aug 23-04:03	4.629	4.080	11.2	−228.94	g	18.73	0.09	1.80	1.39	191.39	285.49
2019 Aug 28-04:52	4.627	4.145	11.6	−224.02	r	18.34	0.06	1.73	1.54	180.68	269.98
2019 Aug 28-04:53	4.627	4.145	11.6	−224.02	r	18.37	0.06	1.78	1.54	175.75	262.63
2019 Aug 28-05:28	4.627	4.146	11.6	−223.99	r	18.43	0.06	1.56	1.71	166.38	248.63
2019 Aug 28-05:29	4.627	4.146	11.6	−223.99	r	18.51	0.06	1.68	1.72	154.56	230.97
2019 Aug 29-04:45	4.627	4.159	11.7	−223.05	r	18.37	0.06	2.22	1.53	177.51	265.38
2019 Aug 29-04:46	4.627	4.159	11.7	−223.05	r	18.43	0.07	2.42	1.53	167.97	251.11
2019 Aug 29-05:46	4.627	4.159	11.7	−223.00	r	18.37	0.06	1.60	1.86	177.51	265.38
2019 Aug 29-05:46	4.627	4.159	11.7	−223.00	r	18.38	0.06	1.62	1.87	175.88	262.95
2019 Aug 29-06:13	4.627	4.159	11.7	−222.99	g	18.85	0.14	1.96	2.13	180.81	270.31
2019 Sep 02-03:50	4.625	4.212	12.0	−219.17	g	18.94	0.11	1.84	1.43	172.19	257.81
2019 Sep 02-05:06	4.625	4.213	12.0	−219.12	r	18.56	0.09	2.20	1.70	154.25	230.94
2019 Sep 03-03:40	4.624	4.226	12.0	−218.20	g	18.73	0.14	1.85	1.41	210.23	314.76
2019 Sep 09-03:04	4.622	4.309	12.3	−212.35	g	18.97	0.26	1.95	1.40	176.75	265.04
2019 Sep 09-05:38	4.622	4.311	12.3	−212.25	r	18.65	0.22	2.84	2.23	149.88	224.75
2019 Sep 25-03:09	4.616	4.540	12.5	−196.68	r	18.61	0.12	4.13	1.57	173.11	259.86
2019 Sep 25-04:55	4.616	4.542	12.5	−196.61	g	19.11	0.23	2.74	2.55	173.26	260.09
2019 Oct 01-03:35	4.614	4.628	12.4	−190.78	g	18.95	0.12	2.15	1.67	207.61	311.48
2019 Oct 09-02:21	4.611	4.742	12.2	−182.98	g	19.16	0.25	1.78	1.49	178.27	267.18
2019 Oct 12-02:42	4.610	4.785	12.0	−180.02	r	18.50	0.12	2.11	1.62	208.92	312.79
2019 Oct 16-02:42	4.608	4.840	11.8	−176.09	g	19.09	0.17	2.40	1.70	195.32	292.15
2019 Oct 19-02:09	4.607	4.881	11.6	−173.17	r	18.71	0.12	1.47	1.59	176.65	263.96
2019 Oct 19-02:36	4.607	4.882	11.6	−173.15	g	19.10	0.14	1.94	1.74	195.56	292.23
2019 Oct 22-02:40	4.606	4.922	11.4	−170.20	g	19.14	0.15	2.32	1.852	190.28	284.07
2019 Oct 26-02:30	4.605	4.975	11.1	−166.27	g	19.42	0.22	3.93	1.891	148.68	221.69
2019 Oct 26-02:35	4.605	4.975	11.1	−166.27	r	18.57	0.12	2.23	1.935	205.24	306.01
2019 Nov 08-01:48	4.601	5.135	9.9	−153.51	r	18.60	0.19	2.13	1.755	204.05	302.88

Note. Columns: (1) observation date; (2) heliocentric distance; (3) topocentric distance; (4) phase angle; (5) difference between time of observation T and time of perihelion T_p; (6) filter; (7) 2×10^4 km aperture mag; (8) 1σ mag uncertainty; (9) in-image seeing of observations; (10) air mass of observations; (11) A(0°)$f\rho$ of observations; (12) cross section of observations.

2.5. Mount Laguna Observatory 40 inch Telescope

Multiband optical images of P/2019 LD$_2$ were obtained with the 1.0 m Telescope at the Mount Laguna Observatory (Smith & Nelson 1969) on 2020 May 17 UTC. Johnson–Cousins B, V, and R filters were used in combination with the E2V 42–40 CCD camera to obtain seven to nine 120 s exposures in each filter. The seeing conditions were 1″92, the air mass was 1.49, and sidereal tracking was used. This facility is a member of the GROWTH collaboration.

2.6. Liverpool Telescope

Observations of P/2019 LD$_2$ were made in g, r, i, and z filters by the 2 m Liverpool Telescope located at the Observatorio del Roque de los Muchachos on 2020 May 29 UTC. The IO:O wide-field camera was used with a 2×2 binning, providing a pixel scale of 0″3 (Steele et al. 2004).

Two 30 s exposures were made per filter with the telescope tracking at the sidereal rate. The seeing conditions were 1″21, and the air mass was 1.75. Detrending of data was performed using the automated IO:O pipeline software (Steele et al. 2004). This facility is a member of the GROWTH collaboration.

2.7. Lulin Optical Telescope

Multiband B, V, and R imaging of P/2019 LD$_2$ was made by the 1 m Lulin Optical Telescope on 2020 June 23–27 UTC and 2020 July 10 UTC. The observations were made using the $2K \times 2K$ SOPHIA camera with a pixel scale of 0″52 (Kinoshita et al. 2005). Exposure times of 90 s were where the telescope was tracked at the nonsidereal rate determined by the ephemeris of the comet. The seeing conditions of the observations were ~1″5, and the air mass was ~1.15.

2.8. Keck I Telescope

A spectrum of P/2019 LD$_2$ was obtained using the Low-Resolution Imaging Spectrometer (LRIS; Oke et al. 1995) on the Keck I telescope on 2020 August 19 UTC (PI J. von Roestel, C272). The blue camera consisting of a $2 \times 2K \times 4K$ Marconi CCD array was used with the red camera consisting of a science-grade Lawrence Berkeley National Laboratory $2K \times 4K$ CCD array. Both cameras have a spatial resolution of 0.″135 pixel^{-1}. We used the 560 nm dichroic with ∼50% transmission efficiency in combination with the 600/4000 grism for the blue camera, rebinned twice in both the spectral and spatial directions, and the 600/7500 grating for the red camera, rebinned once in the spectral direction and twice in the spatial direction, providing a spectral resolution of 0.8 nm and 0.5 nm, respectively, and a spatial resolution of 0.″27. A total integration time of 300 s was used for the exposure and was obtained at air mass 1.″8 in 0.″85 seeing conditions. Both telluric correction and solar-analog stars were observed at air masses similar to that of P/2019 LD$_2$. Wavelength calibration was completed using the HgCdZn lamps for the blue camera and the ArNeXe lamps for the red camera. We used a local solar-analog star to remove the solar component from the spectrum of P/2019 LD$_2$. The LPipe spectroscopy reduction package was used to reduce the data (Perley 2019).

3. Results

3.1. Morphology and Nucleus

Serendipitous prediscovery observations of P/2019 LD$_2$ were obtained with ZTF on 2019 April 26 UTC consisting of three 30 s exposures in the r band. These prediscovery data of P/2019 LD$_2$ have been coadded into a composite image with an equivalent 90 s integration time presented in the top left panel of Figure 1. The comet has an extended appearance with a ∼20″ long tail with a position angle of ∼260° in the antisolar direction. ZTF obtained prediscovery detections of P/2019 LD$_2$ on 2019 April 9, 15, and 20, but the comet did not have a discernible extended appearance in these data.

On 2019 September 7 UTC, the ARC 3.5 m was used to obtain 20×120 s exposures of P/2019 LD$_2$ in the r band. A composite median stack with an equivalent exposure time of 2400 s is presented in the top panel of Figure 1. In the ARC 3.5 m images, the comet has a diffuse, nonstellar appearance. The tail is not easily defined in the ARC 3.5 m median stack, though the comet's extended appearance is enhanced in the opposite direction of the comet's orbital motion with a position angle of ∼230° and length of 5″.

The center panel of Figure 1 presents the appearance of P/2019 LD$_2$ in a median stack of five 380 s F350LP images with an equivalent integration time of 1900 s taken with HST/WFC3 on 2020 April 01 UTC. Cosmic rays have been removed from the composite image stack, with median interpolation of the surrounding pixels. The high-resolution composite HST stack was taken when the comet was at an orbit-plane angle of ∼−0°.44 and had a tail with a length of ∼32″ limited by background structure caused by galaxies and sky noise opposite to the solar direction with a position angle of ∼250°. The ∼32″-long tail translates into a length of 6.2×10^8 m given its topocentric distance of 5.02 au and a phase angle of 10°.7. An enhanced version of the HST median composite stack normalized by the distance from the optocenter reveals a possible jet structure ∼1″ long, as seen in the bottom
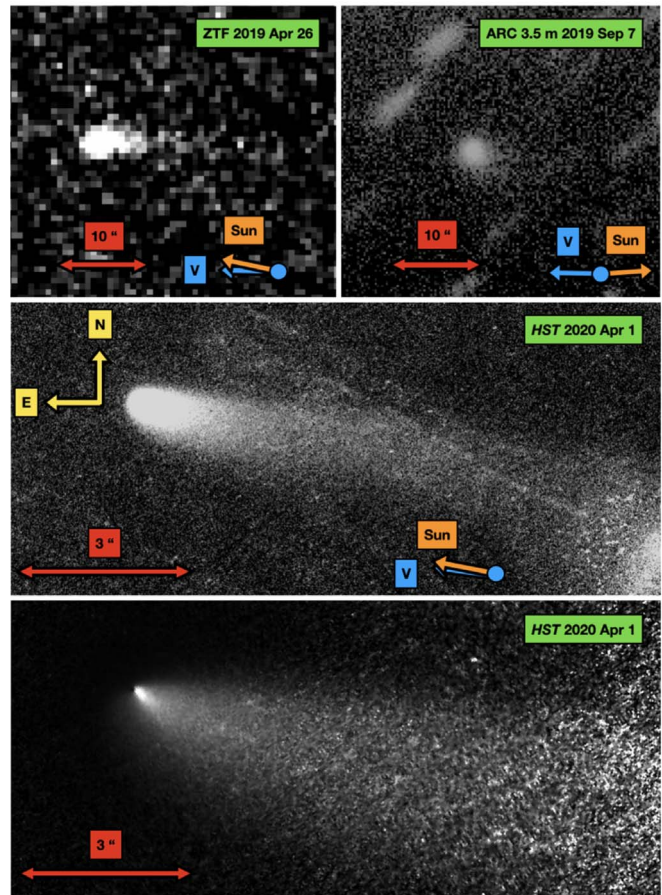
Figure 1. Top left panel: a 90 s equivalent exposure time stack of 3×30 s r-filter images of P/2019 LD$_2$ taken by ZTF on 2019 April 26 UTC. The image stack was compiled using the ZChecker software (Kelley et al. 2019). The pixel scale is 1″/pixel, and the seeing was ∼2.″2. An arrow indicating a width of 10″ is shown for scale, equivalent to ∼30,000 km at the geocentric distance of 4.15 au of the comet on 2020 April 26 UTC. The solar, orbital velocity, and cardinal directions are indicated. Top right panel: a 2400 s equivalent exposure time robust mean stack of 20×120 s r-filter images of P/2019 LD$_2$ taken with the ARC 3.5 m telescope on 2019 September 7 UTC. The telescope was tracked at the comet's motion. The pixel scale is 0.″228 pixel^{-1} and the seeing was ∼1.″4. An arrow indicating a width of 10″ is shown for scale, equivalent to ∼31,000 km at the geocentric distance of 4.28 au of the comet on 2020 September 7 UTC. Center panel: a 1900 s equivalent exposure time robust mean stack of 5×380 s F350LP filter images of P/2019 LD$_2$ taken with HST/WFC3 on 2020 April 1 UTC. The pixel scale is 0.″04/pixel. An arrow indicating a width of 3″ is shown for scale, equivalent to ∼11,000 km at the geocentric distance of 5.02 au of the comet on 2020 April 1 UTC. Bottom panel: the same as the center panel but normalized according to the radial profile of the comet. A ∼1″ jet-like structure is seen with a position angle of ∼210°.

panel of Figure 1. We will discuss the implications of the comet's morphology from these observations for its dust properties in Section 3.3.

We compare the surface-brightness profile of P/2019 LD$_2$ to the simulated surface-brightness profile of a G2 field star WFC3 point-spread function (PSF) assuming the use of the F350LP filter using the TinyTim software (Krist et al. 2011), as seen in Figure 2. The radial profiles of both P/2019 LD$_2$ and the simulated stellar G2V source are computed by azimuthally averaging concentric apertures centered on the optocenter separated by the pixel scale allowed by WFC3 using the F350LP filter. The normalized surface-brightness profile of P/2019 LD$_2$ between 0.″24 and 1.″2 was fit to the functional form of $\Sigma \propto \theta^m$, where Σ is the surface brightness and θ is the
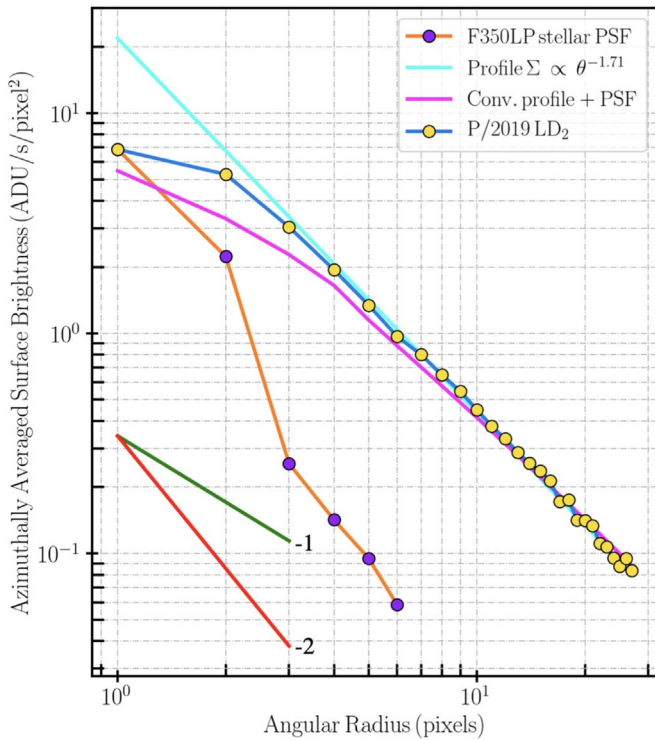
Figure 2. Normalized surface-brightness profile of P/2019 LD$_2$ taken with HST/WFC3 on 2020 April 1 UTC presented as yellow circles with a connecting blue line. A surface-brightness profile of $\Sigma \propto \theta^{-1.71}$ fitted to the profile of P/2019 LD$_2$ between $0\rlap{.}''24$ and $1\rlap{.}''20$ is plotted as the cyan line using the same vertical scale as the the normalized surface-brightness profile of P/2019 LD$_2$. The normalized surface-brightness profile of a F350LP stellar PSF assuming a G2V-like source generated using TinyTim (Krist et al. 2011) is plotted as purple circles with a connecting orange line. The surface-brightness profile resulting from the convolution of the F350LP stellar PSF and the fitted $\Sigma \propto \theta^{-1.71}$ surface-brightness profile of P/2019 LD$_2$ is plotted as a pink line using the same vertical scale as the the normalized surface-brightness profile of P/2019 LD$_2$. Logarithmic surface-brightness gradients with $m = -1$ and $m = -2$ are plotted as green and red lines, respectively, for comparison. Statistical error bars on the surface brightness computed assuming Poissonian statistics at each radius element are smaller than the plot symbols used for both P/2019 LD$_2$ and the synthetic stellar PSF.

distance from the optocenter in pixels, resulting in a radial profile slope of m ~ -1.71. We note that the radial profile slope is steeper than the typical -1 to -1.5 radial profile slope of comets with an isotropic coma in a steady state. The steeper radial profile slope of P/2019 LD$_2$ compared to comets with isotropic coma may be an independent indication of the comet's evolving dust production rate (Jewitt & Meech 1987).

The fitted $0\rlap{.}''24$–$1\rlap{.}''2$ radial profile of P/2019 LD$_2$ was convolved with the synthetic G2V PSF and subtracted from the measured radial profile of P/2019 LD$_2$ to calculate a equivalent nucleus brightness of $V = 22.6 \pm 0.04$ assuming a m$_V$-m$_{F350LP}$ ~ 0.1 (Bolin et al. 2020b). We assume the following phase function for determining the absolute magnitude of the nucleus, H:

$$H = V - 5 \log_{10}(r_h \Delta) - \Phi(\alpha) \qquad (2)$$

where r_h, Δ, and α are the heliocentric distance, topocentric distance, and phase angle of the comet as listed in Table 1 for the 2020 April 1 UTC observation. Here, $\Phi(\alpha) = 0.04\alpha$, where we assume a phase coefficient of 0.04 in magnitudes/degree, resulting in $H = 15.53 \pm 0.05$. The true phase coefficient of

P/2019 LD$_2$ is unknown, so our uncertainty on the measured value of H is considered a lower limit.

From our measured value of H, we calculate the light-scattering cross section, C, of P/2019 LD$_2$ in km^2 using the following function:

$$C = 1.5 \times 10^6 \, p_v^{-1} \, 10^{-0.4H} \qquad (3)$$

where p_v is the albedo of the nucleus, assumed to be ~ 0.08, the typical albedo measured for Centaurs (Bauer et al. 2013), resulting in $C = 11.15 \pm 0.42$ km^2. Converting our measured cross section to a radius using $r = (C/\pi)^2$, we obtain a radius of ~ 1.8 km, comparable to the radius estimates of P/2019 LD$_2$ based on unresolved photometry and the nondetection of P/2019 LD$_2$ from ground-based observations (Schambeau et al. 2020). We note that this is a radius estimate based on a single observation and represents a size assuming a spheroidal shape. Significant deviations from a spheroidal shape, such as a bilobal (Nesvorný et al. 2018) or elongated shape (Bolin et al. 2018; Hanuš et al. 2018) as has been observed for other comet-like bodies, may require additional observations to be made of P/2019 LD$_2$ to accurately determine its size.

3.2. Photometry and Lightcurve

Using the combination of our ground-based observations with the ARC 3.5 m taken on 2019 September 7 UTC, the MLO 1.0 m on 2020 May 27 UTC, the LT on 2020 May 29 UTC, and the Lulin Optical Observatory on 2020 July 10 UTC, we have calculated the mean colors of P/2019 LD$_2$ using 10,000 km photometric apertures of g–$r = 0.60 \pm 0.03$, r–$i = 0.18 \pm 0.05$, and i–$z = 0.01 \pm 0.07$. The filter configuration and viewing geometry of our observations are presented in Table 1. The equivalent angular size of the 10,000 km used in our photometric calculations ranged from $3\rlap{.}''2$ to $3\rlap{.}''7$, with the seeing during observations ranging from $1\rlap{.}''2$ to $1\rlap{.}''9$. We used the color transformations from Jordi et al. (2006) to convert the BVR Johnson–Cousins photometry of P/2019 LD$_2$ from the MLO 1.0 m and LT to the Sloan Digital Sky Survey (SDSS) system.

Our visible measured colors of P/2019 LD$_2$ are reddish to neutral in the ~ 480 nm to ~ 910 nm wavelength range covered by our filters, which is consistent with the measured colors of other active solar system comets as presented in Figure 3. For comparison purposes only, we have included the colors of inactive objects in Figure 3. We note that the measured colors of P/2019 LD$_2$ from our observations are somewhat bluer than the colors of active and inactive Centaurs measured by Jewitt (2015), though this may be due to the longer wavelength coverage of our observations, which go as far as ~ 910 nm, compared to the shorter visible-wavelength observations of Jewitt (2015).

Images from each of the Spitzer DDT program 14331 AORs 1, 4, 6, 9, and 10 that were used to take images of P/2019 LD$_2$ from 2020 January 25 2:23 to 23:11 UTC were reduced using the reduction methods described in Fernández et al. (2013). Images obtained during each of these five AORs using the 4.5 μm channel were coadded to form a single composite image with an equivalent exposure time of 948 s for each AOR.

P/2019 LD$_2$ was located in a crowded star field at a galactic latitude of $\sim -18°$. Therefore, due to the imperfections in the shadowing technique, we used an aperture size with an angular
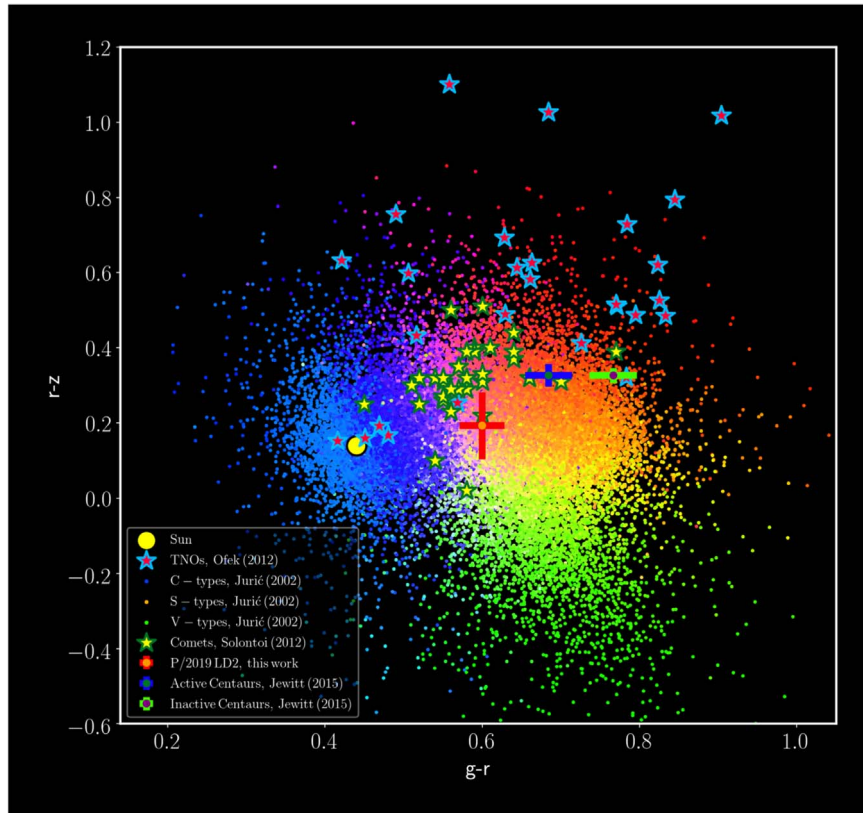
Figure 3. $g - r$ vs. $r - z$ colors of P/2019 LD$_2$ plotted with $g - r$ and $r - z$ colors of inactive solar system C-, S-, and V-type asteroids (Ivezić et al. 2001; Jurić et al. 2002; DeMeo & Carry 2013), active comets (Solontoi et al. 2012), and Kuiper Belt objects (Ofek 2012). The colorization scheme of data points for asteroids by their *griz* colors is adapted from Ivezić et al. (2002). The colors of active and inactive Centaurs from Jewitt (2015) are also included. The most appropriate color comparison between the color of P/2019 LD$_2$ and other solar system bodies is between the active comets in Solontoi et al. (2012) and the active Centaurs from Jewitt (2015) because the colors of P/2019 LD$_2$ are most representative of its dust rather than bare nucleus. The colors of inactive bodies are included for comparison purposes only.

width of $3\rlap{.}''24$, equivalent to 10,000 km at the topocentric distance of 4.26 au of the comet from Spitzer. We obtain an on-source flux density for P/2019 LD$_2$ of 35.6 ± 2.8 μJy at 4.5 μm using the average of the five photometry measurements from the composite images made from each of the AORs 1, 4, 6, 9, and 10. The comet has a slightly extended appearance of more than $\sim 2\rlap{.}''4$ as seen in Figure 4, and an aperture correction was applied to the flux density measurement. The flux from the nucleus assuming a kilometer-scale nucleus radius as measured in Section 3.1 is ~ 0.1 μJy, less than 1% of the total flux.

We present the A$f\rho$ based on the Spitzer/IRAC photometry of P/2019 LD$_2$ using the A$f\rho$ definition of A'Hearn et al. (1984), which is a quantity in units of length, in this case centimeters, that corrects the comet's brightness with respect to heliocentric distance, geocentric distance, aperture size, solar spectrum, and filter wavelength. The values A$f\rho$ are normalized to $0°$ phase angle, $A(0°)f\rho$, using the Halley–Marcus cometary phase function defined by Schleicher & Bair (2011). Assuming that the entirety of the flux in the 4.5 μm Spitzer/IRAC observations is from dust in local thermal equilibrium, we calculate $A(0°)f\rho = 334$ cm. This is strictly an upper limit on $A(0°)f\rho$, due to the possible contribution of gas in the measured flux of the comet.

If we assume that the entirety of the flux from the comet is from CO emission and that the gas speed is 0.5 km s^{-1}, we measure a gas production rate of $1.6 \pm 0.1 \times 10^{27}$ mol s^{-1}, which is similar to the results of Kareta et al. (2020b). For CO$_2$, assuming that the entirety of the flux is due to gas emission, we
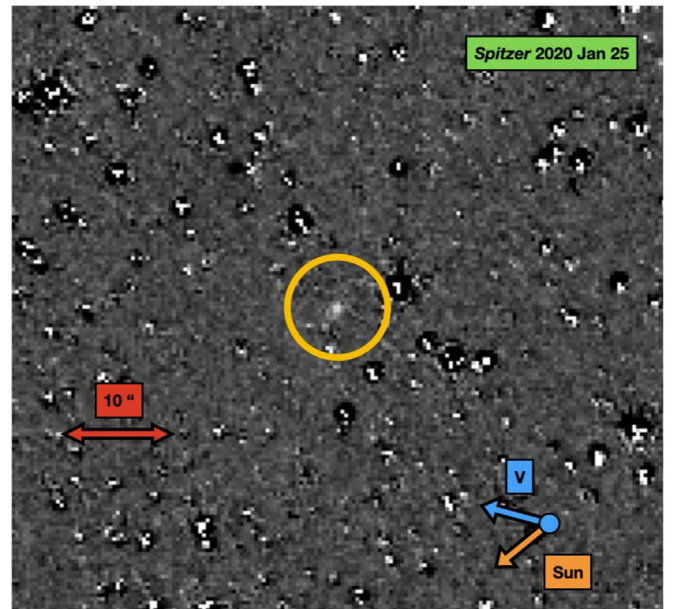
Figure 4. A 948 s equivalent integration time composite image stack made from Spitzer/IRAC observations of P/2019 LD$_2$ taken during Spitzer DDT program 14331 AOR 1 on 2020 January 25 02:23:32 UTC. The detection of P/2019 LD$_2$ has been encircled in yellow. The pixel scale is $1\rlap{.}''2$ pixel^{-1}. An arrow indicating the width of $10''$ is shown for scale, equivalent to $\sim 31,000$ km at the topocentric distance of 4.256 au of the comet on 2020 January 25 UTC. The solar, orbital velocity, and cardinal directions are indicated.
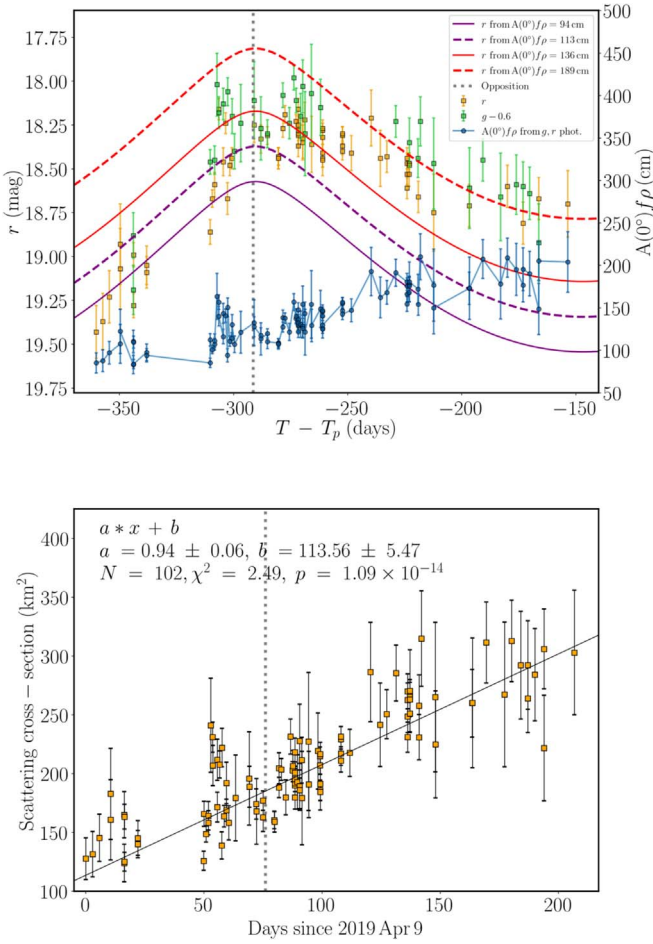
Figure 5. Top panel: g- and r-band photometric lightcurve of P/2019 LD$_2$ versus time from perihelion $(T - T_p)$ measured using a fixed 20,000 km aperture between 2019 April 9 UTC and 2019 November 8 UTC using the data from Table 2. Multiple lines of $A(0°)f\rho = 94$ cm, 113 cm, 136 cm, 189 cm are shown as purple and red solid and dashed lines to reflect the change in the comet's brightness as the comet moved through opposition at $(T - T_p) = -291.5$ days on 2019 June 24 UTC, which is shown as a vertical gray dotted line. In addition, values of $A(0°)f\rho$ calculated using the brightness values and viewing geometry in Table 2 are presented as dark blue data points connected by a light blue solid line. Bottom panel: scattering cross section of P/2019 LD$_2$ calculated using Equation (3) as a function of days since 2019 April 09 UTC from the photometric data presented in Table 2. The black line shows the minimized χ^2 fit to the cross-sectional measurements, and the vertical dashed–dotted line corresponds to the date when P/2019 LD$_2$ was at opposition on 2019 June 24 UTC.

obtain a gas production rate of $1.4 \pm 0.1 \times 10^{26}$ mol s^{-1}, which is comparable to the CO$_2$ measured for comets observed in the MIR at similar heliocentric distances (Reach et al. 2013; Bauer et al. 2015).

Using our archival observations of P/2019 LD$_2$ from ZTF taken between 2019 April 9 UTC and 2019 November 8 UTC, we have plotted the equivalent r magnitudes of P/2019 LD$_2$ as a function of time since the perihelion date of 2020 April 10 UTC, $(T - T_p)$, measured with equivalent 20,000 km apertures and presented in the top panel of Figure 5 with observational details in Table 2. These observations include data taken in the g band, which have been corrected to an equivalent r-band magnitude using our g–r color estimate for P/2019 LD$_2$ of ∼0.6. The 20,000 km aperture was equivalent to an angular size of $5\rlap{.}''4$ on 2019 November 8 UTC, when the

comet had a geocentric distance of 5.14 au and an angular size of $7.52''$, and when the comet had a geocentric distance of 3.67 au on 2019 July 1 UTC. The measured local seeing in the ZTF images at the time of observation ranged between $1\rlap{.}''6$ and $3\rlap{.}''9$ with a median seeing value of $2\rlap{.}''0$. Using only the r-band photometry, the data show a secular brightening trend of the comet as the comet approached opposition on 2019 June 24.42 UTC and was increasing in brightness by $1.6 \pm 0.2 \times 10^{-2}$ mags/day. After leaving opposition, the comet showed an asymmetrical secular fading trend of $0.4 \pm 0.1 \times 10^{-2}$ mags/day compared to the preopposition brightening trend.

In addition to photometry, we present the A$f\rho$ based on the ZTF photometry of P/2019 LD$_2$ as implemented by Mommert et al. (2019). The values A$f\rho$ are normalized to 0° phase angle, $A(0°)f\rho$, and are plotted against the second Y-axis in the top panel of Figure 5 and presented in Table 2. Values of constant $A(0°)f\rho$ are plotted for reference in the top panel of Figure 5. The value of $A(0°)f\rho$ rises consistently over the span of our observations, resulting in asymmetry in the brightness of P/2019 LD$_2$ as it passed through opposition on 2019 June 24 UTC $(T - T_p = -291$ days). Before opposition, between $T - T_p = -370$ and -312, the error-weighted mean of $A(0°)$ $f\rho = 93.9 \pm 11.8$ cm, and between $T - T_p = -312$ and -291, $A(0°)f\rho = 113.1 \pm 8.57$ cm. After opposition, the error-weighted mean of $A(0°)f\rho$ between $T - T_p = -291$ and -211 equaled 136.2 ± 9.7 cm, and from $T - T_p = -211$ and -50, $A(0°)$ $f\rho = 188.8 \pm 25.8$ cm. The range of $A(0°)f\rho$ from 85 cm to 200 cm is consistent with the observed A$f\rho$ range of comets, which ranges from 1 to 10,000 cm (A'Hearn et al. 1995).

3.3. Dust Properties and Mass Loss

In addition to calculating the $A(0°)f\rho$ of P/2019 LD$_2$, we calculate the value of C for each of the equivalent r-band magnitudes in Table 2 using Equation (3), which are plotted in the bottom panel of Figure 5. A linear function is fit to these data, resulting in a fitted slope parameter value of $dC/dt = 0.94 \pm 0.06$ km^2/day. The change in phase angle over the time of our observations is modest, as seen in Table 2, so variations in the phase function used to calculate C should have a minimal effect on the estimate of the uncertainty of our measured slope parameter. Extrapolating backward in time beyond the range of our data results in $C = 0$ km^2 at ∼135 days before 2019 April 9 UTC, the date of our first photometry data point, or on 2018 November 24 UTC, during which P/2019 LD$_2$ had a heliocentric distance of ∼4.8 au, when water ice begins to sublimate (Lisse et al. 2019).

The dimensionless ratio of solar radiation and gravitational forces is defined by β (Burns et al. 1979):

$$\beta = \frac{2L_0 r_H^2}{g_\odot(1au)t^2} \qquad (4)$$

where L_0 is the length of dust travel, in this case, the observed length of the tail of P/2019 LD$_2$ of 6.2×10^8 m; r_H is the heliocentric distance; $g_\odot(1au)$ is the gravitational acceleration toward the Sun at 1 au equal to 6.0×10^{-3} m/s^2; and t is the time of particle release. Assuming a mean value of $r_H \sim 4.6$ au, $L_0 = 6.2 \times 10^8$ m, the length of the tail estimated from the 2020 April 1 UTC HST/WFC3 images, and $t = 4.3 \times 10^7$ s, the time between the 2020 April 1 UTC HST/WFC3 observations and the estimated start of the activity, we calculate a value of
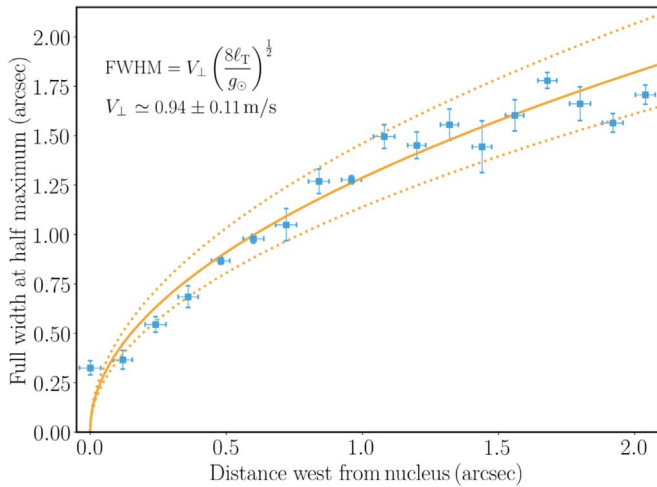
Figure 6. FWHM of the dust tail of P/2019 LD$_2$ versus the westward angular distance, ℓ_T, from the nucleus optocenter of P/2019 LD$_2$ plotted as blue data points when the comet was observed at a $-0°.44$ topocentric and target orbital plane angle with HST/WFC3 on 2020 April 1 UTC. The best-fit line in ℓ_T versus FWHM space according to Equation (5) with $V_\perp = 0.94 \pm 0.11$ m s^{-1} is plotted as an orange line.

$\beta = 2.4 \times 10^3$. Making the assumption that the dust particles are dielectric spheres (Bohren & Huffman 1983), we find that the reciprocal of our estimated value of β translates into a particle size, $\bar{a}$, of ~ 400 μm. However, we caution that this may be an upper limit on the dust size because of the limitations of our tail length measurement by the contamination of background galaxies in the HST/WFC3 images due to variations in the activity of P/2019 LD$_2$ affecting our estimate of t based on the backward extrapolation of the photometric data.

Assuming our estimated particle size of ~ 400 μm, we estimate the total mass loss over the duration of our ZTF observations between 2019 April 9 UTC and 2019 November 8 UTC as $M = 4/3 \, \rho\bar{a}\Delta C$, where ΔC is the difference between the cross sections at the start and end of our observations and is equal to 220 km^2. Assuming a dust density of 1 kg m^{-3} (McDonnell et al. 1986), we obtain a total mass loss over the time span of our observations of $\sim 10^8$ kg. Adopting our estimated value of $dC/dt \sim 1$ km^2/day, we obtain a mass-loss rate using $\dot{M} = 4/3\rho\bar{a} \, dC/dt \sim 5 \times 10^5$ kg/day.

To estimate the fraction of active area of P/2019 LD$_2$, A, we take the ratio between the mass-loss rate and the equilibrium mass sublimation flux at 4.6 au, $f_s = 1.4 \times 10^{-5}$ kg m^{-2} (Jewitt et al. 2015), where $A \sim 0.4$ km^2. Thus, $\sim 10\%$ of P/2019 LD$_2$'s surface is active assuming our inferred size radius of 1.8 km from Section 3.1, comparable to the active surface area measured for Jupiter-family comets (Fernández et al. 1999). An alternative assumption is that P/2019 LD$_2$ has a 100% active area, setting a lower limit to its radius of 0.2 km.

In addition, we use the perpendicular profile of P/2019 LD$_2$ taken with the high-resolution images from HST/WFC3 to estimate the out-of-plane distribution of dust with a minimum of projection effects as the Earth passed through the projected orbital plane of P/2019 LD$_2$ with a projected orbital plane angle of only $0°.4$ on 2020 April 1 UTC. We measured the FWHM along the direction perpendicular to the tail's profile as a function of distance from the optocenter, ℓ_T, between 0 and $\sim 2''$ in increments of $0''.12$ slices, as plotted in Figure 6.
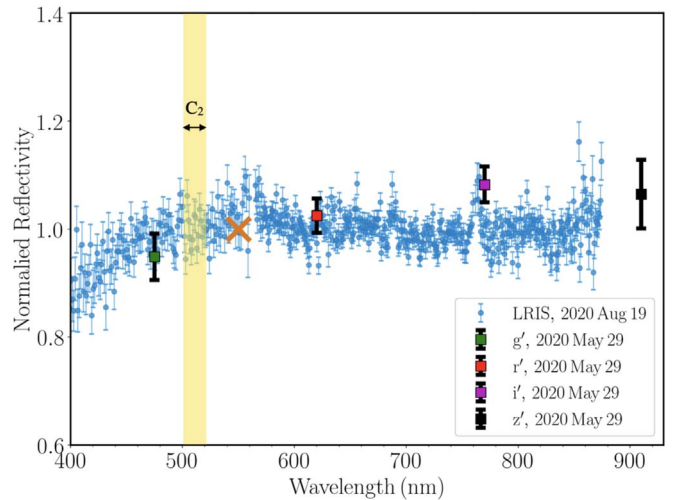
Figure 7. Visible-wavelength reflectance spectrum taken of P/2019 LD$_2$ with the LRIS instrument on Keck I on 2020 August 19 plotted as blue dots. The error bars on the spectrum data points correspond to 1σ uncertainty. The spectrum has been normalized to unity at 550 nm, indicated by the orange cross. The spectrum presented was obtained by combining two spectra from the blue camera using the 600/4000 grism and the red camera using the 600/7500 grating with a 560 nm dichroic (Oke et al. 1995; McCarthy et al. 1998). The data have been rebinned and smoothed by a factor of 10 using an error-weighted mean. The spectral range of the cometary C$_2$ emission line has been indicated by the yellow shaded area (Farnham et al. 2000). The spike in the spectrum at ~ 560 nm is due to an artifact caused by the dichroic solution, and the spike at ~ 760 nm is caused by the telluric H$_2$O absorption feature in both the comet and solar-analog spectra. The data to reproduce our plot of the reflectivity spectrum of P/2019 LD$_2$ are available at the following link: [link].

Neglecting projection effects, the FWHM of the tail gradually widened with ℓ_T and was fit to the function

$$\mathrm{FWHM} = V_\perp \left(\frac{8\ell_T}{g_\odot} \right)^{\frac{1}{2}} \qquad (5)$$

from Jewitt et al. (2014), where $V_\perp$ is the component of the ejection velocity perpendicular to the orbital plane, equal to ~ 1 m s^{-1}. We estimate that the perpendicular component of the ejection velocity scales with $V_\perp \sim 1$ m s^{-1} $(\bar{a}/\bar{a}_0)^{-1/2}$ where $\bar{a}_0 = 400$ μm (Jewitt et al. 2014).

3.4. Spectrum

The spectrum of P/2019 LD$_2$ was extracted using a $7''.4$-wide region centered on the peak of the continuum's brightness. We compute the normalized reflectance spectrum of P/2019 LD$_2$ taken with Keck/LRIS on 2020 August 19 UTC in the wavelength range between 400 nm and 1000 nm by dividing the P/2019 LD$_2$ spectrum by our solar-analog spectrum and normalizing to unity at 550 nm. The resulting spectrum indicates a reddish to neutral coma color for P/2019 LD$_2$, as seen in Figure 7. We measured a slope of $\sim 16\%/$100 nm between 480 and 760 nm and a flatter spectrum between 760 nm and 900 nm consistent with the photometric colors taken by LT on 2020 May 29 plotted over the LRIS spectra in Figure 7 for reference. Our spectrum shows no sign of C$_2$ emission in the 505 nm to 522 nm range (Farnham et al. 2000) in the highlighted range in Figure 7.

We set an upper limit on the C$_2$ gas production of P/2019 LD$_2$ using the mean V-band continuum flux density of P/2019 LD$_2$ using its measured 550 nm flux, flux$_V = 1.52 \times 10^{-15}$

erg cm^{-2} s^{-1} nm^{-1}. The fractional 1σ continuum statistical uncertainty of our P/2019 LD$_2$ spectrum in the range spanning 505 nm to 522 nm is 0.01, corresponding to a 3σ flux density$_{C_2}$ = 2.13×10^{-17} erg cm^{-2} s^{-1} nm^{-1} including a correction of 0.6 for slit losses. The 3σ upper limit to the flux in the 17 nm width of the C$_2$ band is $F_{C_2} \leqslant 3.62 \times 10^{-16}$ erg cm^{-2} s^{-1}. The 3σ upper limit on the number of C$_2$ molecules projected within the $7\rlap{.}''4 \times 1\rlap{.}''0$ spectroscopic slit assuming that the coma is optically thin is

$$N_{mol} = \frac{4\pi\Delta^2 F_{C_2}}{g(r_h)} \qquad (6)$$

where $g(r_h)$ is the fluorescence efficiency factor of the C$_2$ spectral band at r_h where $g(1\,\text{au}) = 2.2 \times 10^{-14}$ erg s^{-1} radical^{-1} (A'Hearn 1982), which results in $N_{mol} \leqslant 1.27 \times 10^{27}$ molecules.

We apply the assumptions of the Haser model (Haser 1957) to determine a coarse 3σ upper limit on the production rate of C$_2$. The Haser model uses two length scales, the "parent" molecule species length scale, L_P, and the "daughter" molecule species length scale, L_D, to describe the distribution of the radicals. For C$_2$ at an r_h of 4.594 au, $L_P = 5.3 \times 10^5$ km and $L_D = 2.5 \times 10^6$ km (Cochran 1985). In addition, we assume the speed of the molecular gas is 0.5 km s^{-1}, which is used to determine the residence time of the molecules in the projected slit (Combi et al. 2004). Using these assumptions with the Haser model, we find the 3σ upper limit to the gas production rate $Q_{C_2} \lesssim 7.5 \times 10^{24}$ mol s^{-1}, which is a similar limit to the measured Q_{C_2} of other solar system comets at similar heliocentric distances (Feldman et al. 2004) and to the results of Licandro et al. (2020). Scaling our measured spectroscopic upper limit on the Q_{C_2} gas production rate to a OH gas production rate using the median ratio of C$_2$ to hydroxyl production rate for solar system comets (A'Hearn et al. 1995) results in an estimated spectroscopic upper limit of $Q_{OH} \lesssim 2.4 \times 10^{27}$ mol s^{-1} and a mass-loss rate in water of $dM_{H_2O}/dt \lesssim 80$ kg s^{-1}.

3.5. Orbital Evolution

In order to investigate the long-term dynamics of 2019 LD$_2$, we simulated 27,000 clones of its orbit. The clone set is created by using 1000 three-dimensional locations using the positional uncertainties. The velocity uncertainties are accounted for by creating 27 clones in the three-dimensional velocity space at each positional location for a total of 27,000 clones. Orbital six-vectors were generated with uncertainties from the JPL Horizons Orbit Solution dated 2020 May 20 at 00:43:28 and set for the 2019 September 15 00:00 UTC epoch. In addition, we use the major gravitational components of the solar system (Sun, Venus, Earth, Mars, Jupiter, Saturn, Uranus, and Neptune). The simulations were conducted using REBOUND (Rein & Liu 2012) with the hybrid MERCURIUS integrator (Rein et al. 2019). We ran two sets of integrations, a short-term set, integrated for 100 yr, and a long-term set for 1×10^7 yr. For each simulation set, we use a time-step size of 0.025 yr. For the long-term integrations, we output every 1000 yr and analyze the time at which the clones escape the solar system (distance from the Sun larger than 1000 au).

The short-term integrations replicate the previous work of Steckloff et al. (2020) and Hsieh et al. (2021). In the simulations, we find that the clones entered the Jovian region

approximately 2.37 yr ago and are ejected from the region 8.70 yr in the future (see the top left panel of Figure 8 for a clone example). As was found previously, 2019 LD$_2$ transitions from a Centaur, with an approximate semimajor axis of 8.6 au, to a Jupiter-family comet with a semimajor axis of 6.2 au, spending 11.0712 yr in the Jovian region (semimajor axis 5.2 au). In the long-term simulations (1×10^7 yr), we find that one-half of the clones escape the solar system in 3.4×10^5 yr and 78.8% of the clones escape the solar system within the first 1×10^6 yr, as seen in the bottom right panel of Figure 8. After $\sim$3.8 Myrs, 95% of the P/2019 LD$_2$ clones have escaped.

4. Discussion and Conclusions

From our observations spanning multiple observatories, transitioning comet P/2019 LD$_2$ exhibits interesting features in comparison with other short-period solar system comets. P/2019 LD$_2$ has a higher value of Afρ of 85–200 cm (A'Hearn et al. 1995) at a heliocentric distance between 4.7 and 4.6 au compared to other short-period comets at a similar heliocentric distance (Kelley et al. 2013; Ivanova et al. 2014; Bauer et al. 2015) and a kilometer-scale nucleus (Fernández et al. 2013), as well as reddish to neutral color properties (Jewitt 2015). The comet's morphology when observed over multiple epochs since 2019 April exhibits the presence of a tail, suggesting sustained activity versus an impulsive event. In addition, P/2019 LD$_2$ has a moderate upper limit for the production of CO and CO$_2$ of $\sim 10^{27}$ mol s^{-1} and $\sim 10^{26}$ mol s^{-1}, respectively, based on our Spitzer observations taken in 2020 January. It is also very active when compared to 29P (although 29P is located at a slightly farther heliocentric distance of $\sim$6 au) on a per unit surface area basis (Af$\rho \sim 150$ cm/(1.8 km)$^2 \sim 50$ cm km^{-2} for P/2019 LD$_2$ versus Af$\rho \sim 1000$ cm/(30.5 km)$^2 \sim 1$ cm km^{-2} for 29P; Ivanova et al. 2011), using the latest value for SW1's size from Schambeau et al. (2019). But this activity seems to produce quite large ($\sim$100 μm), reddish dust particles containing copious amounts of water ice according to our work and that of Kareta et al. (2020b).

In addition to the morphology of the comet indicating sustained activity, the photometry of the comet observed between 2019 April and 2019 November by ZTF is consistent with the activity steadily increasing since late 2018 up through the end of 2019 and into 2020 as the comet nears its perihelion on 2020 April 10 UTC. The length of the tail in deep HST imaging as well as our inferred start date of activity of late 2018 implies that the coma consists of $\sim$100 μm-scale dust ejected at a relatively low velocity of $\sim$1 m s^{-1}. Although this is roughly consistent with the escape speed of a nonrotating comet nucleus of radius $\sim$1.8 km as inferred by our observations, it is unlikely that the dust is being ejected exclusively by the rotational mass shedding suggested by the low ejection velocity (e.g., Ye et al. 2019; Lin et al. 2020). Rather, the increased activity of the comet as it nears perihelion suggests that dust is being transported by the sublimation, or that the activity is a product of both the sublimation of volatiles and rotational mass shedding.

The size of the active region on P/2019 LD$_2$ of $\sim$0.4 km^2 is too large to explain the low ejection velocity of the dust as for other comets with low dust ejection velocities whose activity is driven by the sublimation of volatiles (Jewitt et al. 2014). Subsequent observations of P/2019 LD$_2$ to determine the rotation state of the comet will be necessary to understand if it is rotating near its critical rotation limit, indicating the role of
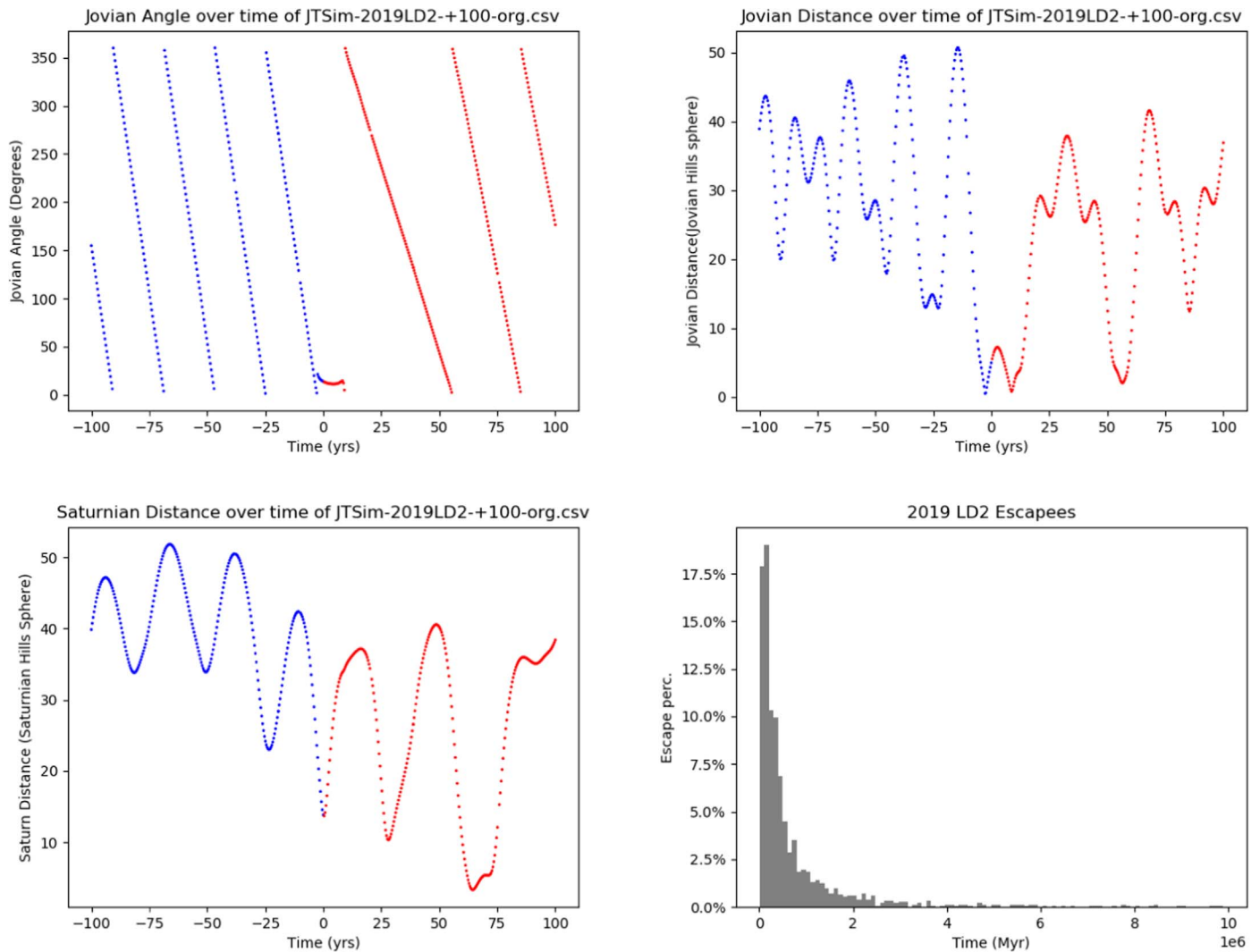
Figure 8. Top left panel: Jovian angle defined as the relative longitude between Jupiter and P/2019 LD$_2$ as a function of time between -100 and 100 yr centered on 2019 September 15 UTC. Except for a brief period of time between -3 and 8 yr where the Jovian angle was $\sim20°$, the Jovian angle cycled between 0° and 360°. Top right panel: same as the top left panel except for the Jovian distance defined as the distance between P/2019 LD$_2$ and Jupiter in Jovian Hill spheres (~0.35 au) as a function of time. The local minimum in the Jovian distance occurred ~2.77 yr ago with a distance of ~0.50 Jovian Hill radius, or 0.17 au. Bottom left panel: same as the top right panel except for the Saturn distance defined as the distance between P/2019 LD$_2$ and Saturn in Saturn Hill spheres (0.43 au). The local minimum occurs in ~60 yr when P/2019 LD$_2$ comes within ~3.3 Hill radii or 1.42 au of Saturn. Bottom right panel: percentage of orbital P/2019 LD$_2$ clones that have escaped the solar system (reached >1000 au from the Sun) per bin in duration of time. Each bin is $\sim100,000$ yr wide. Within the first million years of the simulation, $\sim78.8\%$ have escaped the solar system. By 10 million years, $\sim95\%$ have escaped the solar system.

rotational mass shedding in its activity or if the comet has the possibility of becoming rotationally disrupted in the near future or if it was disrupted in the recent past (Moreno et al. 2017; Vokrouhlický et al. 2017). Given the 4–5 au location of the comet during its recent epoch of activity, the distance at which water ice begins to sublimate (Meech & Svoren 2004), it is likely that the activity is being driven primarily by the sublimation of water ice. An additional possible mechanism may be the transformation of amorphous water ice into crystalline water, as has been suggested as an activity-driving mechanism for Centaurs (Jewitt 2009). It is possible for other volatiles such as CO to partially drive the activity of P/2019 LD$_2$, as seen in other distant comets (e.g., Bolin et al. 2020b) and 29P (Gunnarsson et al. 2008), but the lack of detection of the activity at large heliocentric distances (Schambeau et al. 2020) seems to suggest that hypervolatiles are not the dominant drivers of the activity of P/2019 LD$_2$. If the lack of hypervolatiles driving the activity of P/2019 LD$_2$ is confirmed,

it may suggest that P/2019 LD$_2$ has spent a significant amount of time as a Centaur within 15 au of the Sun (Horner et al. 2004b), where these hypervolatiles may have had a greater chance to become depleted compared to water ice, which is nonvolatile at that distance.

Additionally, some comets show evidence of a strong transition between H$_2$O-driven and CO-driven activity at heliocentric distances past ~3.5 au, such as for comets 67P (Läuter et al. 2019) and Hale-Bopp (Biver et al. 1997). Our observation of the activity of P/2019 LD$_2$ and its inferred H$_2$O-driven activity at its heliocentric distance of ~4.6 au at the time of our observations is seemingly at odds with the transition to CO-driven activity at larger heliocentric distances as observed for other comets. However, it has been shown that the shape and rotation pole orientation of comets can have a strong effect on the distance at which comet activity is driven by H$_2$O. H$_2$O-driven activity can increase at larger heliocentric distances for comet shapes and orientations deviating from a

spherically shaped comet rotating perpendicular to its orbital plane (Marshall et al. 2019). Therefore, the inferred H_2O-driven activity of P/2019 LD_2 at its large heliocentric distance of 4.6 au could be explained by it having a nonspherical shape and significant obliquity, which has been shown to sustain H_2O activity at these heliocentric distances in comet-activity models.

P/2019 LD_2 is beginning to enter the region where water ice begins to appreciably sublimate at rates high enough that a patch of pure water ice in the surface would disappear on year-long timescales. The beginnings of mobilization of water ice for a weakly structured surface such as found on 67P (O'Rourke et al. 2020) could lead to the slow flaking off of large chunks of the loosest, weakest material that had never felt such stresses before. In this scenario, gas will evolve at low levels in order to drive dust off the object. The material driven off should be rich in water ice, as this ice is the last, most refractory ice expected in a cometary body before it is totally depleted of volatile ice. We then may expect to see P/2019 LD_2's activity modulated by its motion toward or away from the Sun over an orbit similar to how the activity of Main Belt Comets are modulated as they travel inside or outside the 2.5 au water "ice line," where water ice boils furiously into vacuum (Hsieh et al. 2015a, 2015b); P/2019 LD_2's activity could be modulated by its traversing the water ice turn-on line of activity. Future monitoring observations over the next years will determine if this is the case, as is suggested by the smoothly increasing A$f\rho$ toward perihelion values we find for P/2019 LD_2; they do not appear to be describing an impulsive outburst.

In our long-term simulations (1×10^7 yr), we show the temporary nature of 2019 LD_2. Up to 78.8% of our orbital clones escape in the first 1×10^6 yr. The half-life of the clones is approximately 3.4×10^5 yr. This is an order of magnitude smaller than the mean half-life of Centaurs (2.7×10^6 yr; Horner et al. 2004b) and more comparable to the lifetimes of Jupiter-family group comets of $\sim 5 \times 10^5$ yr (Levison & Duncan 1994).

Without a robust assessment of survey selection effects (e.g., Jedicke et al. 2016; Boe et al. 2019), it is difficult to assess the true population of comets in a temporary co-orbital configuration with Jupiter and transitioning between the Centaur and Jupiter-family comet populations (Sarid et al. 2019). However, we can use our estimated size of P/2019 LD_2 in comparison with the population estimates of Centaurs in the transition region (Steckloff et al. 2020). Steckloff et al. (2020) predict that there are ~ 40–1000 objects in the transition region with radius >1–3 km, and fewer if cometary fading is considered in the population estimate (Brasser & Wang 2015). Using these transition-object population estimates and our estimate of the radius of P/2019 LD_2 of ~ 1.8 km suggests that there are ~ 100 objects the size of P/2019 LD_2 in the transition region at any given time. Additional monitoring of P/2019 LD_2 and objects like it in the gateway region will be required to understand their activity drivers and population.

Facilities: Hubble Space Telescope, Spitzer Space Telescope, Keck I Telescope, P48 Oschin Schmidt telescope/Zwicky Transient Facility, Apache Point Astrophysical Research Consortium 3.5 m telescope, Liverpool Telescope, Lulin Optical Telescope, Mount Laguna Observatory 40 inch Telescope.

Software: Small Body Python, ZChecker, LPipe, REBOUND.

ORCID iDs

Bryce T. Bolin ⓘ https://orcid.org/0000-0002-4950-6323
Yanga R. Fernandez ⓘ https://orcid.org/0000-0003-1156-9721
Carey M. Lisse ⓘ https://orcid.org/0000-0002-9548-1526
Timothy R. Holt ⓘ https://orcid.org/0000-0003-0437-3296
Zhong-Yi Lin ⓘ https://orcid.org/0000-0003-3827-8991
Kunal P. Deshmukh ⓘ https://orcid.org/0000-0001-5253-3480
James M. Bauer ⓘ https://orcid.org/0000-0001-9542-0953
Eric C. Bellm ⓘ https://orcid.org/0000-0001-8018-5348
Dennis Bodewits ⓘ https://orcid.org/0000-0002-2668-7248
Kevin B. Burdge ⓘ https://orcid.org/0000-0002-7226-836X
Sean J. Carey ⓘ https://orcid.org/0000-0002-0221-6871
Chris M. Copperwheat ⓘ https://orcid.org/0000-0001-7983-8698
George Helou ⓘ https://orcid.org/0000-0003-3367-3415
Jonathan Horner ⓘ https://orcid.org/0000-0002-1160-7970
Varun Bhalerao ⓘ https://orcid.org/0000-0002-6112-7609
Chan-Kao Chang ⓘ https://orcid.org/0000-0003-1656-4540
Christine Chen ⓘ https://orcid.org/0000-0002-8382-0447
Mansi M. Kasliwal ⓘ https://orcid.org/0000-0002-5619-4938
Frank J. Masci ⓘ https://orcid.org/0000-0002-8532-9395
Chow-Choong Ngeow ⓘ https://orcid.org/0000-0001-8771-7554
Robert Quimby ⓘ https://orcid.org/0000-0001-9171-5236
Michael Coughlin ⓘ https://orcid.org/0000-0002-8262-2924
Richard Dekany ⓘ https://orcid.org/0000-0002-5884-7867
Dmitry A. Duev ⓘ https://orcid.org/0000-0001-5060-8733
Matthew Graham ⓘ https://orcid.org/0000-0002-3168-0139
Thomas Kupfer ⓘ https://orcid.org/0000-0002-6540-1484
Russ R. Laher ⓘ https://orcid.org/0000-0003-2451-5482
Ashish Mahabal ⓘ https://orcid.org/0000-0003-2242-0244
Przemyslaw J. Mróz ⓘ https://orcid.org/0000-0001-7016-1692
Reed Riddle ⓘ https://orcid.org/0000-0002-0387-370X
Roger M. Smith ⓘ https://orcid.org/0000-0001-7062-9726
Maayane T. Soumagnac ⓘ https://orcid.org/0000-0001-6753-1488
Lin Yan ⓘ https://orcid.org/0000-0003-1710-9339

References

A'Hearn, M. F. 1982, in Comets, ed. L. L. Wilkening (Tucson, AZ: Univ. Arizona Press), 433
A'Hearn, M. F., Millis, R. C., Schleicher, D. O., Osip, D. J., & Birch, P. V. 1995, Icar, 118, 223
A'Hearn, M. F., Schleicher, D. G., Millis, R. L., Feldman, P. D., & Thompson, D. T. 1984, AJ, 89, 579
Bauer, J. M., Grav, T., Blauvelt, E., et al. 2013, ApJ, 773, 22
Bauer, J. M., Stevenson, R., Kramer, E., et al. 2015, ApJ, 814, 85
Bellm, E. C., Kulkarni, S. R., Graham, M. J., et al. 2019, PASP, 131, 018002
Biver, N., Bockelée-Morvan, D., Colom, P., et al. 1997, EM&P, 78, 5
Boe, B., Jedicke, R., Meech, K. J., et al. 2019, Icar, 333, 252
Bohren, C. F., & Huffman, D. R. 1983, Absorption and Scattering of Light by Small Particles (New York: Wiley)
Bolin, B., Fernandez, Y., Bauer, J., Helou, G., & Lisse, C. 2019, Spitzer investigation of the first known active Trojan, 2019 LD2, Spitzer Proposal 14331
Bolin, B. T., Bodewits, D., Fernandez, Y., & Lisse, C. M. 2020a, Determining the cause of activity of the first active Trojan, 2019 LD2, HST Proposal 16077
Bolin, B. T., & Lisse, C. M. 2020, MNRAS, 497, 4031
Bolin, B. T., Lisse, C. M., Kasliwal, M. M., et al. 2020b, AJ, 160, 26
Bolin, B. T., Weaver, H. A., Fernandez, Y. R., et al. 2018, ApJL, 852, L2
Brasser, R., & Wang, J. H. 2015, A&A, 573, A102
Burns, J. A., Lamy, P. L., & Soter, S. 1979, Icar, 40, 1
Chandler, C. O., Kueny, J. K., Trujillo, C. A., Trilling, D. E., & Oldroyd, W. J. 2020, ApJL, 892, L38
Cochran, A. L. 1985, AJ, 90, 2609
Combi, M. R., Harris, W. M., & Smyth, W. H. 2004, in Comets II, ed. M. C. Festou, H. U. Keller, & H. A. Weaver (Tucson, AZ: Univ. Arizona Press), 523
De Sanctis, M. C., Capria, M. T., Coradini, A., & Orosei, R. 2000, AJ, 120, 1571
DeMeo, F. E., & Carry, B. 2013, Icar, 226, 723
Deustua, S. E., Mack, J., Bajaj, V., & Khandrika, H. 2017, WFC3/UVIS Updated 2017 Chip-Dependent Inverse Sensitivity Values, Instrument Science Rep. WFC3 2017-14
Dones, L., Brasser, R., Kaib, N., & Rickman, H. 2015, SSRv, 197, 191
Dressel, L. 2012, Wide Field Camera 3 Instrument Handbook for Cycle 21 v. 5.0 (Baltimore, MD: STScI)
Duncan, M., Levison, H., & Dones, L. 2004, in Comets II, ed. M. C. Festou, H. U. Keller, & H. A. Weaver (Tucson, AZ: Univ. Arizona Press), 193
Farnham, T. L., Schleicher, D. G., & A'Hearn, M. F. 2000, Icar, 147, 180
Fazio, G. G., Hora, J. L., Allen, L. E., et al. 2004, ApJS, 154, 10
Feldman, P. D., Cochran, A. L., & Combi, M. R. 2004, in Comets II, ed. M. C. Festou, H. U. Keller, & H. A. Weaver (Tucson, AZ: Univ. Arizona Press), 425
Fernández, J. A., Tancredi, G., Rickman, H., & Licandro, J. 1999, A&A, 352, 327
Fernández, Y. R. 2009, P&SS, 57, 1218
Fernández, Y. R., Kelley, M. S., Lamy, P. L., et al. 2013, Icar, 226, 1138
Fitzsimmons, A., Young, D., Armstrong, J., Moss, S., & Sato, H. 2020, COMET P/2019 LD2 (ATLAS), Minor Planet Electronic Circulars MPEC 2020-K134, https://www.minorplanetcenter.net/mpec/K20/K20KD4.html
Gladman, B., Marsden, B. G., & Vanlaerhoven, C. 2008, in The Solar System Beyond Neptune, ed. M. A. Barucci et al. (Tucson, AZ: Univ. Arizona Press), 43
Graham, M. J., Kulkarni, S. R., Bellm, E. C., et al. 2019, PASP, 131, 078001
Gunnarsson, M., Bockelée-Morvan, D., Biver, N., Crovisier, J., & Rickman, H. 2008, A&A, 484, 537
Hanuš, J., Delbo, M., Alí-Lagoa, V., et al. 2018, Icar, 299, 84
Haser, L. 1957, BSRSL, 43, 740
Horner, J., & Evans, N. W. 2006, MNRAS, 367, L20
Horner, J., Evans, N. W., & Bailey, M. E. 2004a, MNRAS, 355, 321
Horner, J., Evans, N. W., & Bailey, M. E. 2004b, Mon. Not.R. Astron. Soc., 354, 798
Horner, J., & Lykawka, P. S. 2012, MNRAS, 426, 159
Hsieh, H. H., Denneau, L., Wainscoat, R. J., et al. 2015a, Icar, 248, 289
Hsieh, H. H., Fitzsimmons, A., Novaković, B., Denneau, L., & Heinze, A. N. 2021, Icar, 354, 114019
Hsieh, H. H., Hainaut, O., Novaković, B., et al. 2015b, ApJL, 800, L16
Huehnerhoff, J., Ketzeback, W., Bradley, A., et al. 2016, Proc. SPIE, 9908, 99085H
Ivanova, O., Borysenko, S., & Golovin, A. 2014, Icar, 227, 202
Ivanova, O. V., Skorov, Y. V., Korsun, P. P., Afanasiev, V. L., & Blum, J. 2011, Icar, 211, 559
Ivezić, Ž, Tabachnik, S., Rafikov, R., et al. 2001, AJ, 122, 2749
Jedicke, R., Bolin, B., Granvik, M., & Beshore, E. 2016, Icar, 266, 173
Jewitt, D. 2015, AJ, 150, 201
Jewitt, D., Hsieh, H., & Agarwal, J. 2015, in Asteroids IV, ed. P. Michel, F. E. DeMeo, & W. F. Bottke (Tucson, AZ: Univ. Arizona Press), 221
Jewitt, D., Ishiguro, M., Weaver, H., et al. 2014, AJ, 147, 117
Jewitt, D. C. 2009, AJ, 137, 4296
Jewitt, D. C., & Meech, K. J. 1987, ApJ, 317, 992
Jordi, K., Grebel, E. K., & Ammon, K. 2006, A&A, 460, 339
Jurić, M., Ivezić, Ž, Lupton, R. H., et al. 2002, AJ, 124, 1776
Kareta, T., Volk, K., Noonan, J. W., et al. 2020a, RNAAS, 4, 74
Kareta, T., Woodney, L. M., Schambeau, C., et al. 2020b, arXiv:2011.09993

Kasliwal, M. M., Cannella, C., Bagdasaryan, A., et al. 2019, PASP, 131, 038003

Kelley, M. S., Fernández, Y. R., Licandro, J., et al. 2013, Icar, 225, 475

Kelley, M. S. P., Bodewits, D., Ye, Q., et al. 2019, in ASP Conf. Ser., 523, Astronomical Data Analysis Software and Systems XXVII, ed. P. J. Teuben et al. (San Francisco, CA: ASP), 471

Kinoshita, D., Chen, C.-W., Lin, H.-C., et al. 2005, ChJAA, 5, 315

Krist, J. E., Hook, R. N., & Stoehr, F. 2011, Proc. SPIE, 8127, 81270J

Läuter, M., Kramer, T., Rubin, M., & Altwegg, K. 2019, MNRAS, 483, 852

Levison, H. F., & Duncan, M. J. 1994, Icar, 108, 18

Licandro, J., Pinilla-Alonso, N., de Leon, J., et al. 2020, AAS/DPS Meeting, 52, 404.06

Lin, Z.-Y., Cheng, Y.-L., Vincent, J.-B., et al. 2020, PASJ, 72, 79

Lisse, C., Bauer, J., Cruikshank, D., et al. 2020, NatAs, 4, 930

Lisse, C. M., Young, L. A., Cruikshank, D., Sandford, S., & Schmitt, B. 2019, Icar, submitted

Ivezić, Ž, Lupton, R. H., Jurić, M., et al. 2002, AJ, 124, 2943

Marshall, D., Rezac, L., Hartogh, P., Zhao, Y., & Attree, N. 2019, A&A, 623, A120

Marzari, F., Scholl, H., Murray, C., & Lagerkvist, C. 2002, in Asteroids III, ed. W. F. Bottke, Jr. et al. (Tucson, AZ: Univ. Arizona Press), 725

Masci, F. J., Laher, R. R., Rusholme, B., et al. 2019, PASP, 131, 018003

McCarthy, J. K., Cohen, J. G., Butcher, B., et al. 1998, Proc. SPIE, 3355, 81

McDonnell, J. A. M., Alexander, W. M., Burton, W. M., et al. 1986, Natur, 321, 338

Meech, K. J., & Svoren, J. 2004, in Comets II, ed. M. C. Festou, H. U. Keller, & H. A. Weaver (Tucson, AZ: Univ. Arizona Press), 317

Mommert, M., Kelley, M., de Val-Borro, M., et al. 2019, JOSS, 4, 1426

Morbidelli, A., Levison, H. F., Tsiganis, K., & Gomes, R. 2005, Natur, 435, 462

Moreno, F., Pozuelos, F. J., Novaković, B., et al. 2017, ApJL, 837, L3

Murray, C. D., & Dermott, S. F. 1999, Solar System Dynamics (Cambridge: Cambridge Univ. Press)

Nesvorný, D., Parker, J., & Vokrouhlický, D. 2018, AJ, 155, 246

Nesvorný, D., Vokrouhlický, D., Dones, L., et al. 2017, ApJ, 845, 27

Ofek, E. O. 2012, ApJ, 749, 10

Oke, J. B., Cohen, J. G., Carr, M., et al. 1995, PASP, 107, 375

O'Rourke, L., Heinisch, P., Blum, J., et al. 2020, Natur, 586, 697

Perley, D. A. 2019, PASP, 131, 084503

Reach, W. T., Kelley, M. S., & Vaubaillon, J. 2013, Icar, 226, 777

Rein, H., Hernandez, D. M., Tamayo, D., et al. 2019, MNRAS, 485, 5490

Rein, H., & Liu, S.-F. 2012, A&A, 537, A128

Roig, F., & Nesvorný, D. 2015, AJ, 150, 186

Sarid, G., & Prialnik, D. 2009, M&PS, 44, 1905

Sarid, G., Volk, K., Steckloff, J. K., et al. 2019, ApJL, 883, L25

Sato, H., Heinze, A., & Nakano, S. 2020, CBET, 4780, 1

Schambeau, C., Fernandez, Y., Belton, R., et al. 2020, CBET, 4821, 1

Schambeau, C. A., Fernández, Y. R., Samarasinha, N. H., Woodney, L. M., & Kundu, A. 2019, AJ, 158, 259

Schleicher, D. G., & Bair, A. N. 2011, AJ, 141, 177

Smith, C. E., & Nelson, B. 1969, PASP, 81, 74

Solontoi, M., Ivezić, Ž, Jurić, M., et al. 2012, Icar, 218, 571

Steckloff, J. K., Sarid, G., Volk, K., et al. 2020, ApJL, 904, L20

Steele, I. A., Smith, R. J., Rees, P. C. T., et al. 2004, Proc. SPIE, 5489, 679

Tonry, J. L. 2011, PASP, 123, 58

Vokrouhlický, D., Nesvorný, D., & Dones, L. 2019, AJ, 157, 181

Vokrouhlický, D., Pravec, P., Durech, J., et al. 2017, A&A, 598, A91

Werner, M. W., Roellig, T. L., Low, F. J., et al. 2004, ApJS, 154, 1

Ye, Q., Kelley, M. S. P., Bodewits, D., et al. 2019, ApJL, 874, L16